School of Physics and Astronomy

Using Bessel-Gaussian Beam in Optical Trapping of Nanoparticles for Sensitive Gravimetry

By

Md Iftekher Selim Chowdhury

Master of Research Literature Review

A thesis submitted to Macquarie University in partial fulfillment of the requirements for admission to the degree of Master of Research in Physics

Supervisor: Dr. Gabriel Molina-Terriza

July 04, 2017

ORIGINALITY STATEMENT

'I hereby declare that this submission is my own work and to the best of my knowledge it contains no materials previously published or written by another person. I also declare that it contains no substantial proportions of material have been accepted for the award of any other degree or diploma at Macquarie University or any other educational institution, except where due acknowledgement is made in the thesis. I explicitly acknowledged in the thesis, any contribution made to the research by others, with whom I have worked at Macquarie University or elsewhere. I also declare that the intellectual content of this thesis is the product of my own work, except to the extent that assistance from others in the project's design and conception or in style, presentation and linguistic expression is acknowledged.'

Signed _____

Date 04/07/2017

Acknowledgements

I would like to take this opportunity to express my earnest gratitude to Dr. Gabriel Molina-Terriza for supervising me in this project. It has been exciting journey working with him and learning from him. He has been very generous with his time in guiding me and enlightening me with the science of quantum-optical trapping and levitation and I sincerely hope that the results from this project would eventually make positive contributions to the science of sensitive gravimetry.

A very special thanks goes to Reece Roberts. He has been a true mentor and a constant guide in this relentless journey of optical trapping of neutral particles. Without his constant guidance, knowledge sharing and assistance, this journey would have proved quite challenging.

Also, very special thanks go to Mathieu Juan and Xavier Vidal Asensio, both had been a true mentor. They always had their door open for me. They were always kind and patient with me allowing me to constantly bombard them with questions. Their knowledge and assistance in Optical alignment techniques has been invaluable to me.

Finally, my special gratitude towards Richard Neo for guiding me and assisting me in learning the use of Spatial Light Modulator (SLM) and LabView.

I would also like to express my gratitude towards Xavier Zambrana for sharing his SLM Labview code for generating Bessel beam.

Abstract

Over the past decade, researchers have developed very sensitive force detection techniques including yoctonewton ($10^{-24}N$) force measurement, yoctogram-scale mass sensitivity and femto-scale magnetic field sensing. However, the measurement of gravitational or inertial forces to such high precision still to date remains a scientific and technological challenge. Compact integrated room temperature inertial sensors capable of sensing ultra-small changes in inertial forces is still lacking.

In this thesis, I propose an all-optically controlled novel design for performing sensitive gravimetry based on trapped and levitated nanoparticles using Bessel-Gaussian beams. I particularly focus on the characterization of Bessel-Gaussian beam and its challenges and application in optical trapping.

Optical trapping in vacuum and air has near-complete mechanical isolation from the environment. Without the need for clamping mechanism and robust decoupling from surrounding environment, the all-optical trapping and cooling techniques will yield potentially ultrahigh Q-factor resulting in ultrasensitive force detection at room temperature.

Table of Contents

Chapter 1

Introduction and Motivation

1.1 Introduction

Arthur Ashkin of Bell laboratories in 1970 first pioneered and laid down the foundation of the study of optical forces through his landmark experiment. He demonstrated that with tightly focused beams of light, it is possible to generate a radiation pressure force and accelerate tiny dielectric particles. During his experiment, he also made an unanticipated observation that along with accelerating the particles, it is also possible to trap those particles within the tightly confined focus of the beam. His work was published in a series of seminal papers discussing his observations on guiding particles with radiation pressure (Ashkin, 1970), deflecting atoms with radiation pressure (Ashkin, 1970), levitating particles with radiation pressure (Ashkin et al, 1971), levitating airborne droplets (Ashkin et al, 1975), levitating particles in high vacuum (Ashkin et al, 1976), precision trapping with feedback stabilization (Ashkin et al, 1977a), and observing resonances in radiation pressure (Ashkin et al, 1977b) among others. The seminal papers were complemented with relative classical theories addressing his experimental results. Ashkin in 1970 also pointed out that a laser beam can exert significant scattering force on an atom and consequently raising the possibility of trapping atoms (Ashkin, 1970) and as such greatly influenced the coming days of the development of the field of atom trapping. Inspired by Ashkin's work, there was a development of the study of atom trapping. This inevitably led to a drive to cool the motion of atoms inside the trap. The laser cooling and laser trapping of atoms are two distinct processes but they are certainly interrelated. In optical trapping of atoms, where the trapping techniques are applied to the induced dipole of optical transition states, to be discussed shortly, the primary challenge is to provide a stable trap. This is because the potential wells of the trap are very shallow, only a few kelvin deep, giving rise to the possibility for the atoms to escape the trap with sufficient thermal energy above this value. A brief introduction to the trapping potential would be useful at this stage. A particle at the focus of a laser beam will feel a trapping potential such that whenever the particle is displaced from the focus, a restoring force, i.e. gradient force, will push the particle inside the trap. The potential well has to compete with the external temperature of the surrounding medium, i.e. due to collisions of different atoms, which tends to shake the particle from its trapped position.

Therefore, the atoms must be pre-cooled below this temperature before the trapping could begin.

In 1985, Chu et al demonstrated the confinement and cooling of atoms (Chu et al, 1985) also known as optical molasses. It was in 1986 when Chu et al first reported the experimental observation of optical trapping of neutral sodium atom (Chu et al, 1986). Since 1985, there had been significant work in the field of optical cooling of neutral atoms to achieve stable atom trap which include velocity selective coherent population trapping (Coheh-Tannoudji et al, 1988), sideband cooling (Wineland et al, 1989) and Sisyphus cooling (Coheh-Tannoudji et al, 1989) and opened the door to an entirely new field of research known as cold atom physics. Their work has contributed to two Nobel prizes to date in the field of optical cooling and trapping. In 1997, Nobel prize was awarded to Steven Chu, Claude Cohen-Tannoudji and William D. Phillips for development of methods of laser cooling and trapping of atoms (Chu, 1998) and influenced by their work in 2001, a Nobel prize was awarded to Eric A. Cornell, Wolfgang Ketterle and Carl E. Wieman for the creation Bose-Einstein condensates in cold atomic gases (Ketterle, 2002).
To this end, it is important to briefly address the readers about the relation between classical trapping and atom trapping, the inherent challenge resulting from their relations and the potential doors to new research fields. Both classical trapping and atom trapping phenomenon are the realization of the same force which is essentially the interaction of the polarizability, describing the field induced dipole strength, of the trapped particle/atom with the applied electric field of trapping beam. But there is a significant difference between these two distinct trapping phenomena. In classical trapping, the force interacts with the dipole moment of the particle induced by the applied electric field. Whereas, in atom trapping, the force interacts with induced dipole which arises due to the distinct energy states present in the electronic structure in the atoms. Hence these two trapping phenomena exists in entirely two different regimes. Now this inevitably brings about a big challenge of applying the confirmed cooling techniques from atom trapping to the cooling of the center of mass motion of nano-particles in classical trapping. This challenge results due to the absence of distinct energy states in these microscopic systems in classical trapping. By inserting artificial impurities in microscopic system, such a Nitrogen Vacancy (NV) center in diamond, we can marry these two phenomena from two distinct domains and borrow the cooling techniques from atom trapping to cool center of mass motion in classical trapping (L. Giannelli et all, 2016).

Meanwhile as much of the work on laser cooling of atoms flourished, in 1986 Ashkin et al reported observation of stable traps of dielectric particles with strongly focused single-beam gradient force (Ashkin et al, 1986) also known “Optical Tweezers”. This optical trapping

technique was soon to be used to trap and manipulate viruses and bacteria (Ashkin et al, 1987a and Ashkin et al, 1987b) and had since found many of its applications in biological sciences.
The optical levitation of dielectric particles has attracted a lot of attention in recent times (D. E. Chang et al, 2010; O. Romero-Isart et al, 2010; Tongcang Li et al, 2010; P. F. Barker et al, 2010; P. f. Barker, 2010; T. Li et al, 2011; P. Asenbaum, 2013). Not to mention that optical levitation had had a humble beginning during the early pioneering days of optical trapping compared to the rich range of applications that trapping in aqueous medium enjoyed. Optical trapping is controlling the motion of a particle with optical field by creating these optical potentials. Of course, the optical trapping potential again, as mentioned earlier, has to compete with the stochastic forces due to the collision with the atoms in the medium that the particle is trapped. This gives rise to two very different regimes. Optical trapping in overdamped systems and optical trapping in underdamped systems. In overdamped regimes, this collision dominates the physics of the system so the particle does not have enough energy to oscillate. While in the underdamped regimes, there is not so much collision with the particle. Which means there is no friction and the particle can oscillate freely acting as a harmonic oscillator. In particular, these two regimes appear naturally in two different systems i.e. when trapping is performed in aqueous medium and when trapping is performed in air. The first system is typically called optical trapping in liquid while the second system is called optical levitation since the particle is free floating. In water, we have the addition of the buoyancy forces because the water is pushing the particle. While in air, we cannot rely on the buoyancy forces and we have to fully compensate for the gravitation forces.

There is a tradeoff when addressing optical trapping in aqueous medium and in air or vacuum. The advantage of trapping in aqueous medium is that of the viscosity of fluid which aids in reducing the particle's motion such that it is easier to trap the particle at the focus of the beam. Whereas, for trapping in air or vacuum, the particle must drift into the focus of the beam with very small or no momentum at all since it lacks the necessary drag force and consequently it is difficult to trap in air or vacuum. But once the particle is stably levitated and trapped in air or vacuum, it has overwhelming advantages over other mechanical systems. This is because the levitated particles can be highly isolated and strongly decoupled (Ashkin, 1970; Ashkin et al, 1971; R. Omori et al, 1997) from its external room-temperature environment. Due to the absence of the mechanical contact with its environment, the decoherence becomes negligible (Zhang-qi Yin, 2009). The oscillation or trapping frequency also becomes fully tunable. This makes such system ideal for studying macroscopic quantum mechanics such as ultrasensitive

sensors for force detection (A. A. Geraci et al, 2010; A. Arvanitaki et al, 2013) including the gravitational wave detection (Arvanitaki et al, 2013).

The past decade was full of great promises in the research field of ultrasensitive force detection. During this period, researchers had developed several extremely sensitive force measurement techniques to measure numerous form of quantities such as nanomechanical mass sensor (yoctogram-scale resolution) using a carbon nanotube mechanical oscillator held at mK temperatures (Chaste et al, 2012), ultrasensitive force detection and displacement (yoctoNewton) using groups of trapped ions (Biercuk et al, 2010), and sub-femtotesla scaler atomic magnetometer using a multi-pass RP vapour cell (Sheng et al, 2012).

Even with such success in ultrasensitive force detection, till to date, it remains a great technological and scientific challenge to measure gravitational or inertial forces to a comparable degree of high precision. It is worth mentioning that during the last decade, we witnessed the revolutionary advancement in the navigation system due to the design of compact, integrated and high-precision inertial sensors. However, we are still lacking a compact, stable and fully integrated ultra-precision inertial sensor capable of measuring ultra-small inertial force changes which can operate at room temperature environment.

This project is a novel attempt, devised at Macquarie University, in the field of research of ultrasensitive force detection. The aim of this project is to lay down the initial foundational work for a novel design of fully-optically controlled inertial sensor operable at room temperature. This work will hopefully pave the way for a sub-nm optical displacement gravity sensing measurement which can be presented to the scientific community.

1.1 Motivation for the project

The groundbreaking technological advancement in Microelectromechanical Systems (MEMS) resulted in compact miniature accelerometers; also, readily available nowadays in cars, smart phones, etc. Standard noise produced in these micro accelerometers is of order $100mg/\sqrt{Hz}$ where $g = 9.8\,m/s^2$. Given the standard maximum allowed integration time and noise in these systems, an overall resolution of few mg is achieved (www.nxp.com). Despite such astounding achievements, these compact accelerometers do not even come close towards meeting the requirements for the resolution needed in precision gravity measurements or gravimetry. The variations of the gravitational field of the earth is of order $\sim\mu g \sim mGal$ $[1Gal \equiv 1cm/s^2]$. To address the need for measuring such local variation of earthly gravitational field in such higher resolution, a sophisticated technology based on the atomic fountain was developed and successfully commercialized.

This technology is essentially measuring the time of flight of free falling atoms via optical interferometry techniques which gives precision of the order of $10ng/\sqrt{Hz}$ (M. Schmidt, 2011, M. Schmidt et al, 2011, M. Angelis et al, 2008, M. K. Zhou et al, 2012). Regrettably designing a commercial compact portable version of this technology, while maintaining high-resolution, offers a serious technological challenge. The smallest volume that most of these standard commercial systems comes in to date, with the aim of maintaining such high precision resolution, is close to cubic meter.

Now we can potentially overcome such limitation by designing a gravimeter solely based on an all-optical technique. Optical levitation of dielectric particles in air or vacuum comes with the advantage of near-complete mechanical isolation with its surrounding environment. Such near-perfect isolation results in potentially enormous mechanical-Q factor. Furthermore, it is possible to cool the particle's center of mass motion using all optical techniques since the particle is levitated in vacuum and it is divorced with its immediate surroundings. A micron-sized dielectric particle can act as a massive (microscopic) dynamical oscillator and optically levitating such particle in vacuum and cooling down the particle will make the particle more sensitive to weak inertial forces.

The main objective of this experimental project is to optically levitate and trap dielectric nano-particles in air and to modulate the trapping frequency to any arbitrary small value. The experimental outcomes of this project will give us better insight into the potential development of an all-optically controlled inertial sensor with the aim of achieving precision that exceeds the value of available commercial gravimeters $\sim \mu g/\sqrt{Hz}$ and hopefully achieve the value of $\sim ng/\sqrt{Hz}$.

Chapter 2

Physics of Optical Trapping and Introduction to Bessel Beams

2.1 A Brief Review of Optical Trapping and Levitation

In this introductory section, a review of the basic physics behind optical trapping is presented. The theories are reproduced from numerous earlier works and books and referenced throughout accordingly. Early in the history of electromagnetism, it was recognized that electromagnetic radiation carries both linear and angular momentum and can exert significant forces and torques on particles. Optical trapping makes use of this fundamental property of light to trap particles in a potential well created by the trapping beam. Optical traps involve two

types of forces such as 1) Scattering force and 2) Gradient force. The scattering force pushes the particle along the propagation direction of the radiation; whereas the gradient force pulls the particle along the spatial gradient of radiation intensity. When the optical gradient force is much stronger than the optical scattering force, the particle is attracted towards the highest intensity point duly formed by the focused beam and thus we can stably trap the particle at this point from all three dimensions (A. Ashkin et al, 1986, J. R. Moffitt et al, 2008).

Both scattering and gradient forces can be understood from the perspective of different approximations that we can make to the trapping phenomenon (Y. Harada et al, 1996, A. Ashkin et al, 1971). Depending on the size of the particle, we can use different approximations and consequently we have different trapping regimes i.e. 1) Geometrical or ray optics regime, 2) Dipole or Rayleigh regime and 3) Multipolar regime. When the diameter of the trapped particle is much larger than the wavelength of the trapping light ($D \gg \lambda$), then the optical trapping phenomenon can be explained using Ray Optics and we are in ray optics regime. Whereas, when the diameter of the trapped particle is much smaller than the wavelength of the trapping light ($D \ll \lambda$), we can apply the limiting approximation called the Dipole or Rayleigh approximation to describe the behavior of a dielectric particle in an electromagnetic field. In the dipole approximation, the dielectric particle can be treated as a simple point dipole induced by the applied electric field. Finally, when the diameter of the trapped particle is comparable to the wavelength of the trapping light, we are in multipolar regime which is the most complex phenomenon of the three. In this experiment, I am going to work in the Rayleigh regime with dielectric particles. Therefore, in the subsequent sections, I will address the trapping forces based on the Rayleigh regimes.

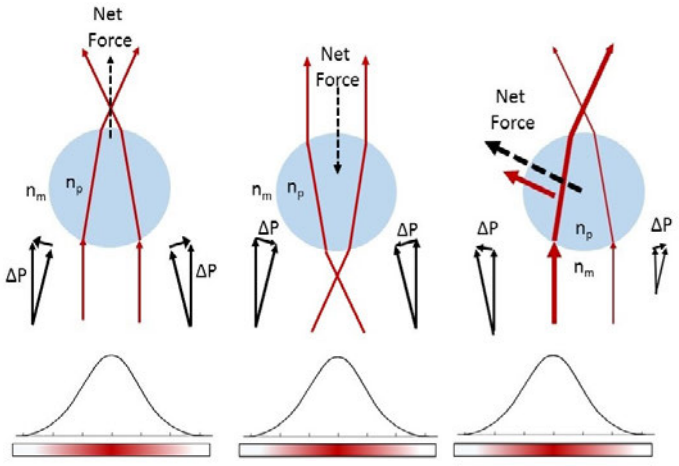

(Figure 2.1: (a) The refraction of rays from the focused Gaussian beam transfers momentum shift and thus a force on the spherical particle. (b) The particle is sitting in the center of the beam above the focal point, hence the net force pushes the particle down towards the focus of the beam. (c) The particle is shifted rightwards transversely to the beam axis. Symmetry is broken, and hence the net restoring force attracts the particle to the left.)

Now in practice, a near-infrared laser beam with Gaussian transverse profile is tightly focused down to a diffraction limited spot using a high-numerical aperture objective such that a large spatial gradient in radiation intensity is created. This region of strong intensity gradient is

essential in forming a stable trap. A stronger intensity gradient will result in a stronger gradient force and as the gradient force becomes much stronger than the scattering force, we move towards more stable trap. Hence the key to a most stable optical trap is this region, center of the focus, where strong intensity gradient is present (J. R. Moffitt et al, 2008). This single beam gradient force trapping is known as "Optical Tweezers" (A. Ashkin et al, 1986).

Intuitively speaking, the trapping forces are simplest to explain in the ray optics regime. Let us consider the index of refraction of the trapped particle. When the refractive index of the trapped particle is higher than the refractive index of the surrounding environment, the particle behaves like a converging lens to the incident rays and the net forces attracts the particle towards the strong intensity gradient region. The opposite is true when the refractive index of the trapped particle is lower than the refractive index of the surrounding environment and the net forces pushes the particle away from the strong intensity gradient region. Figure 2.1 depicts few diagrams from ray optics regimes which give us a qualitative understanding of the force vectors that arise due to a Gaussian beam incident on a particle with higher refractive index

2.2 Optical Forces in Dipole or Rayleigh Regime

Let us begin by looking briefly at the trapping beam profile. A laser beam profile with a fundamental Gaussian mode corresponding to the TEM_{00} mode is used in this experiment. The geometry of the focused Gaussian beam profile is shown in the following figure 2.2:

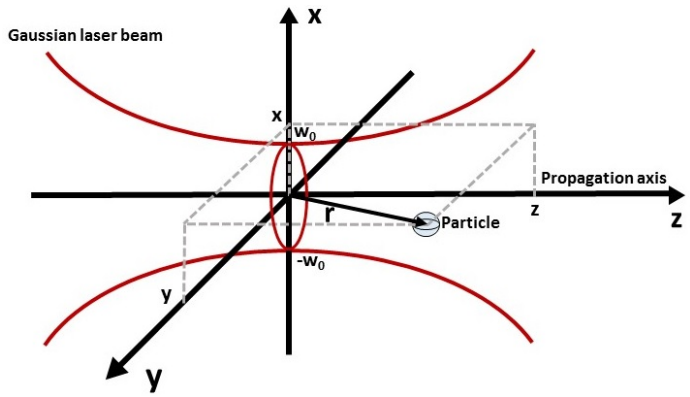

(Figure 2.2: Geometrical depiction of a particle of radius a at a position $r = (x, y, z)$ in focused Gaussian beam of waist w_0.)

Using the zeroth-order approximation in a paraxial Gaussian beam description with linear polarization, the electric field vector at the position r is given by the following formula (Harada et al, 1995):

$$\varepsilon(r,t) = \hat{x}E_0 \frac{ikw_0^2}{ikw_0^2+2z} e^{\left[-\frac{(kw_0)^2(x^2+y^2)}{(kw_0^2)^2+(2z)^2}\right]} e^{-ikz} \times e^{\left[-i\frac{2kz(x^2+y^2)}{(kw_0^2)^2+(2z)^2}\right]} e^{-i\omega t} \quad (2.1)$$

$$= \hat{x}\frac{E_0}{2} e^{-i\emptyset(r)} e^{-i\omega t} \quad (2.2)$$

where $E_0 = \frac{1}{2}\sqrt{\frac{4P}{\pi W_0^2 n_m \epsilon_0 c}}$ is the electric field strength, P is the beam power, $\hat{x}$ is the unit vector along the polarization direction, $k = n_m \frac{\omega}{c}$ is the wave number in the medium, ω is the trapping frequency and w_0 is the beam waist position.

Under this approximation, the associated magnetic field vector is given by the following formula (Harada et al, 1995):

$$H(r,t) = \hat{z} \times \frac{\varepsilon(r,t)}{Z_0} \cong \hat{y} n_m \epsilon_0 c \varepsilon(r,t) = \hat{y} H(r,t) \qquad (2.3)$$

where $Z_0 = \sqrt{\frac{\mu_m}{\epsilon_m}} \cong \frac{1}{(n_m \epsilon_0 c)}$ is the intrinsic impedance of the medium, n_m is the refractive index of the surrounding media, $c = \frac{1}{\sqrt{\epsilon_0 \mu_0}}$ is the speed of light, ϵ_0 is the vacuum permittivity and μ_0 is the vacuum permeability.

An instantaneous energy flux travelling through a unit area per unit time also known as Poynting vector is given by the following formula:

$$S(r,t) \equiv \varepsilon(r,t) \times H(r,t) \qquad (2.4)$$

The irradiance at the position r also known as beam intensity is given by the following formula:

$$I(r) = \| \langle S(r,t) \rangle_T \| = \frac{1}{2} Re[\varepsilon(r,t) \times H^*(r,t)] = \| \tilde{z} \frac{n_m \epsilon_0 c}{2} |E_0(r)|^2 \|$$

$$= \left(\frac{2P}{\pi w_0^2}\right) \frac{1}{1+(2\tilde{z})^2} e^{\left[-\frac{2(\tilde{x}^2+\tilde{y}^2)}{1+(2\tilde{z})^2}\right]} \qquad (2.5)$$

where $(\tilde{x}, \tilde{y}, \tilde{z}) = \left(\frac{x}{\omega_0}, \frac{y}{\omega_0}, \frac{z}{\omega_0^2}\right)$ represents the normalized spatial co-ordinates, P is the beam power.

It must be noted that the above descriptions are making use of the paraxial approximation of Maxwell's equations to the scaler wave equation of the Gaussian beam and these descriptions are only valid when $w_0 \gg \lambda$. For $w_0 \ll \lambda$, these descriptions are valid for only one component of electric and magnetic field and higher order corrections are required (Y. Harada et al, 1996, A. Ashkin et al, 1971). Now a brief description of the dipole force and scattering force will follow.

2.2.1 Gradient Force

This force arises due to the Lorentz force acting on the induced dipole by the electromagnetic field. In the dipole regime, the trapped particle size is much smaller than the wavelength of the trapping light ($D \ll \lambda$) and therefore, the instantaneous electromagnetic field the particle experiences due to the incident beam is taken to be uniform and the electrostatic formulae can be applied. The particle acting as a simple point dipole moment in the instantaneous electric

field is given by the following formula (Y. Harada et al, 1996, J. A. Stratton, 1941, M. Kerker, 1969):

$$\vec{p}(r,t) = \alpha\vec{E}(r,t) = 4\pi n_m^2 \epsilon_0 a^3 \left(\frac{m^2-1}{m^2+2}\right)\vec{E}(r,t) \qquad (2.6)$$

The classical optical force acting on the expectation value of the classical dipole moment $\langle\widehat{D}_\epsilon\rangle$ at position r_0 and driving the motion of a classical particle is given by the following formula (G. Grynberg et al, 2010):

$$F = \langle\widehat{D}_\epsilon\rangle\nabla E(r,t)_{r_0} \qquad (2.7)$$

The particle undergoes forced oscillation at the driving frequency ω of the applied field and therefore we can write the following relation (G. Grynberg et al, 2010):

$$\langle\widehat{D}_\epsilon\rangle = \epsilon_0\alpha\varepsilon + c.c \qquad (2.8)$$

where α is the polarizability of the particle. The polarizability is a complex number and is expressed in the following way:

$$\alpha = \alpha' + i\alpha'' \qquad (2.9)$$

The polarizability depends on the applied frequency, applied field amplitude and has the dimensions of length cubed.

We are taking the internal state of the classical particle to reach a steady state at a given point r_0 under the effect of the applied field (G. Grynberg et al, 2010),

$$E(r,t) = \varepsilon(r,t) + \varepsilon^*(r,t) \qquad (2.10)$$

We already know,

$$\varepsilon(r,t) = \hat{x}\frac{E_0(r)}{2}e^{i\emptyset(r)}e^{-i\omega t} \qquad (2.11)$$

Now substituting equation (2.9) into equation (2.8), we obtain the following four terms (G. Grynberg et al, 2010):

$$F = \epsilon_0\alpha\varepsilon\nabla\varepsilon_{r_0} + \epsilon_0\alpha^*\varepsilon^*\nabla\varepsilon^*_{r_0} + \epsilon_0\alpha\varepsilon\nabla\varepsilon^*_{r_0} + \epsilon_0\alpha^*\varepsilon^*\nabla\varepsilon_{r_0}$$

$$= \epsilon_0\alpha'\frac{E_0(r)}{2}\nabla E_0(r)_{r_0} - \epsilon_0\alpha''\frac{E_0^2(r)}{2}\nabla\emptyset(r)_{r_0} \qquad (2.12)$$

The first two terms oscillate at 2ω and after averaging over time, gives rise to no effects. The remaining two terms do not oscillate at all and hence give rise to a force. Consequently, the radiative force is comprised of only two contributions. One of these contributions is related to the real part α' of the polarizability and depends on the gradient of the intensity or amplitude of the electromagnetic wave. This contribution is called "Dipole Force" or "Gradient Force". Now the remaining contribution is related to the imaginary part α'' of the polarizability and depends on the gradient of the phase of the electromagnetic wave. This contribution is called "Resonance-Radiation Force" which is the resonant scattering force related to the absorption of the photons (G. Grynberg et al, 2010). Now caution must be applied not to confuse this

resonant scattering force due to absorption with the scattering force due to Rayleigh scattering from the particle in classical trapping.

For a small particle in any given medium we have the following relation:

$$\alpha = \alpha' + i \cdot \alpha'' = 4\pi n_m^2 a^3 \left(\frac{m^2-1}{m^2+2}\right) \qquad (2.13)$$

where α is the complex polarizability of the particle to the surrounding medium, n_p is the refractive index of the particle, n_m is the refractive index of the medium and $m = \frac{n_p}{n_m}$ is the relative refractive index of the particle.

Substituting equation (2.13) into equation (2.12), we have the following relation:

$$F_{grad}(r) = Real\left[4\pi n_m^2 \epsilon_0 a^3 \left(\frac{m^2-1}{m^2+2}\right) \frac{E_0(r)}{2} \nabla E_0(r)_{r_0}\right] \qquad (2.14)$$

Our chosen particle for optical trapping are mostly transparent dielectric spheres. Hence the complex component of the polarizability is zero ($\alpha'' = 0$). Consequently, the resonant scattering force due to absorption of the particle is neglected.

From the vector identity $\nabla E^2 = 2(E \cdot \nabla)E + 2E \times (\nabla \times E)$ and using $(\nabla \times E) = 0$ from Maxwell's equations we get the following equations (Y. Harada et al, 1996, J. P. Gordon, 1973):

$$F_{grad}(r) = 4\pi n_m^2 \epsilon_0 a^3 \left(\frac{m^2-1}{m^2+2}\right) \frac{1}{2} \nabla \langle E^2(r,t) \rangle_T$$

$$= \pi n_m^2 \epsilon_0 a^3 \left(\frac{m^2-1}{m^2+2}\right) \frac{1}{2} \nabla |E(r,t)|^2$$

$$= \frac{2\pi n_m^2 a^3}{c} \left(\frac{m^2-1}{m^2+2}\right) \frac{1}{2} \nabla \mathrm{I}(r) \qquad (2.15)$$

Substituting beam intensity from equation (2.5), the gradient or dipole force can be expressed in terms of three following rectangular components:

$$F_{grad,x}(r) = \hat{x} \frac{2\pi n_m^2 a^3}{c} \left(\frac{m^2-1}{m^2+2}\right) \frac{\frac{4\hat{y}}{W_0}}{1+(2\hat{z})^2} \times \left(\frac{P}{\pi w_0^2}\right) \frac{1}{1+(2\hat{z})^2} e^{\left[-\frac{2(\hat{x}^2+\hat{y}^2)}{1+(2\hat{z})^2}\right]} \qquad (2.16)$$

$$F_{grad,y}(r) = \hat{y} \frac{2\pi n_m^2 a^3}{c} \left(\frac{m^2-1}{m^2+2}\right) \frac{\frac{4\hat{x}}{w_0}}{1+(2\hat{z})^2} \times \left(\frac{P}{\pi w_0^2}\right) \frac{1}{1+(2\hat{z})^2} e^{\left[-\frac{2(\hat{x}^2+\hat{y}^2)}{1+(2\hat{z})^2}\right]} \qquad (2.17)$$

$$F_{grad,z}(r) = \hat{z} \frac{2\pi n_m^2 a^3}{c} \left(\frac{m^2-1}{m^2+2}\right) \frac{\frac{8\hat{z}}{kw_0^2}}{1+(2\hat{z})^2} \times \left[1 - \frac{2(\hat{x}^2+\hat{y}^2)}{1+(2\hat{z})^2}\right] \left(\frac{2P}{\pi w_0^2}\right) \frac{1}{1+(2\hat{z})^2} e^{\left[-\frac{2(\hat{x}^2+\hat{y}^2)}{1+(2\hat{z})^2}\right]} \qquad (2.18)$$

For high refractive index particle, the scattering force from equation pushes the particle along the propagation direction only. Whereas, the gradient force consists of three-dimensional force components which acts as a restoring force attracting the particle towards the center of the focused beam which is a high intensity region. The complete opposite is true for particles

with lower refractive index where the particle is pushed away from the center of the focused beam and might get trapped in the minima of local intensity. A generalization of this fact is possible for all beam types.

It can be shown that by integrating equation 2.15, the dipole force can be derived from taking derivative of the following potential:

$$F_{grad}(r) = -\nabla U_{cl}(r) \qquad (2.19)$$

where the potential is as follows:

$$U_{cl} = \frac{2\pi n_m a^3}{c}\left(\frac{m^2-1}{m^2+2}\right)\frac{2P}{\pi w_0^2} \qquad (2.20)$$

To be able to successfully trap a particle, the potential depth needs to be much larger than the average kinetic energy of the particle due to Brownian motion ($K_B T$).

2.2.2 Scattering Force

The realization of classical scattering force is due to the photons having momentum. The force of the scattering photons acts along the propagation direction of the light and is dependent on the intensity of the light. The incident beam photons can be absorbed and reemitted by the particles and therefore, two impulses are received by the particles. The force exerted on the particle is equal to the difference between the momentum transfer of the input beam and the scattered field from the particle i.e. the scattered field due to the induced polarizability. In the dipolar regime, a particle can be treated as a simple point dipole induced by the applied field (section 2.1). As the electromagnetic field oscillates harmonically, the induced dipole follows the polarization direction of the electric field and consequently, the particle acts as an oscillating dipole moment which radiates along all directions in a toroidal shape. Therefore, the momentum impulse from all the directions due to induced dipole averages out to be zero and a net force from momentum impulse due to input beam along the incident beam propagation direction accumulates. This scattering force is given by the following formula (Y. Harada et al, 1996, K. Svoboda et al, 1994, K. Visscher et al, 1992):

$$F_{scat} = \hat{z}\frac{n_m \sigma}{c}\langle S\rangle_T = \hat{z}\left(\frac{n_m}{c}\right)\sigma I(r) \qquad (2.21)$$

where n_m is the refractive index of the surrounding medium, $\langle S\rangle$ is time averaged Poynting vector, c is the speed of light and σ is the scattering cross-section of the particle for radiation pressure. In the Raleigh regime where the small dielectric particles scatter isotopically, the σ is given by the following formula (M. Kerker, 1969):

$$\sigma = \frac{8}{3}\pi(ka)^4 a^2\left(\frac{m^2-1}{m^2+2}\right)^2 \qquad (2.22)$$

where $m = \frac{n_p}{n_m}$ is the relative refractive index of the particle. By substituting equation (2.22) into equation (2.21), the scattering force in terms of intensity distribution of the incident beam is given by the following formula:

$$\hat{F}_{scat}(\hat{r}) = \hat{z}\frac{8}{3}\pi(ka)^4 a^2 \left(\frac{m^2-1}{m^2+2}\right)^2 \times \left(\frac{2P}{\pi\omega_0^2}\right)\frac{1}{1+(2\hat{z})^2} e^{\left[-\frac{2(\hat{x}^2+\hat{y}^2)}{1+(2\hat{z})^2}\right]} \qquad (2.23)$$

We can see from the above expression that the scattering trapping force is strongly dependent on the beam intensity, wavelength and trapped particle size.

2.3 Optical Trapping Frequency

The motion of a trapped particle at the focus of the optical trap due to the trapping forces is conceptually analogous to the scenario of a simple harmonic oscillator. A particle confined within an optical force field acts as a harmonic oscillator. Therefore, the potential energy J stored in the spring:

$$J = \frac{1}{2}\kappa\langle x^2\rangle \qquad (2.24)$$

where κ is the spring or force constant and $\langle x^2\rangle$ is the variance in displacement. Invoking the classical approximation of the equipartition theorem, the energy within the Brownian motion of the trapped particle:

$$\frac{1}{2}k_B T \qquad (2.25)$$

$$\therefore \frac{1}{2}\kappa\langle x^2\rangle = \frac{1}{2}k_B T \qquad (2.26)$$

Therefore, the trapping stiffness:

$$\kappa = \frac{\langle x^2\rangle}{k_B T} \qquad (2.27)$$

The simple calculation of the stiffness involves calculating the variance in displacement which in turn requires an accurately calibrated position detector. The frequency spectrum of the Brownian noise of a particle gives an alternate easier way of calculating the trapping stiffness. Considering the mass of a Silica particle in fluid to be very small, the inertial forces on the particle are much weaker compared to the hydrodynamic drag forces. This statement is true for a levitated Silica particle in air and only breaks down once the levitated particle is placed in vacuum. Hence, the motion of Silica particle is mathematically analogous to that of a massless damped oscillator driven by Brownian motion:

$$\beta\dot{x}(t) + \kappa x(t) = F(t) \qquad (2.28)$$

Where $\beta = 6\pi\upsilon a$ is the drag coefficient of the Silica particle, υ is the viscosity of the immediate surroundings, a is the radius of the Silica particle and $F(t)$ is the force due to Brownian noise.

The frequency spectrum of the Brownian noise source is constant in amplitude and has zero mean:

$$\left|\tilde{F}(f)\right|^2 = 4\beta k_B T \qquad (2.29)$$

Doing the Fourier transform of equation:

$$2\pi\beta\left(\frac{\kappa}{2\pi\beta} - if\right)\tilde{x}(f) = \tilde{F}(f) \qquad (2.30)$$

Consequently, the power spectrum is as follows:

$$|\tilde{x}(f)|^2 = \frac{k_B T}{\pi^2\beta\left[\left(\frac{\kappa}{2\pi\beta}\right)^2 + f^2\right]} \qquad (2.31)$$

Equation is that of a Lorentzian with a corner frequency:

$$f_c = \frac{\kappa}{2\pi\beta} \qquad (2.32)$$

Finally, the trapping stiffness is as follows:

$$\kappa = 2\pi\beta f_c \qquad (2.33)$$

2.3 Measuring Ultra-Small Changes in Inertial Force Using Levitated Dielectric Particles

The levitation and trapping is essentially achieved through the interplay between the scattering force, gradient force and gravity. We already know,

$$F_{opt} = F_{scat} + F_{grad} \qquad (2.34)$$

The acceleration of the levitated dielectric particle due to gravity can be expressed with the following formula:

$$M\ddot{z} = -Mg(t) + F_{opt} = -Mg(t) + F_{scat} + F_{grad} \qquad (2.35)$$

where M is the mass of the particle, $g(t) = g_0 + \Delta g(t)$ is due to the influence of the gravitational force and $g_0 \approx 9.8\, m/s^2$.

Given a certain dynamic range, the gradient force can be treated as a simple harmonic restoring force along a certain direction; that is $F_{grad(x)} = K(x - x_0)$, $F_{grad(y)} = K(y - y_0)$ or $F_{grad(z)} = K(z - z_0)$. Here, x_0, y_0 and z_0 are the equilibrium position in the absence of any external force and K is the restoring constant which is dependent on the gradient of the electromagnetic field along the x, y or z direction via $K = k\frac{\partial I}{\partial x}$, $K = k\frac{\partial I}{\partial y}$ or $K = k\frac{\partial I}{\partial z}$. In this context, the dynamics of gradient force is considered along the x axis. Now, when an equilibrium position is reached due to the interaction between the scattering force, gradient force and gravity, we have:

$$Mg(t) = F_{scat} + F_{grad} = F_{scat} + K(x - x_0) \qquad (2.36)$$

$$\therefore\ x - x_0 = \frac{Mg(t) - F_{scat}}{K} \qquad (2.37)$$

Therefore, to obtain large response from significantly small changes due to any external force, the restoring constant K need to be very small which essentially requires a weak gradient force. We can also see this effect from the relation between trapping frequency f_c and the stiffness of the optical trap which is given by $K = 2\pi\beta f_c$ (Refer to chapter 4). If we lower the trapping frequency f_c, the optical trap stiffness, i.e. the restoring constant K becomes weaker. Which results in a shallow trapping potential and thus, any small change in external forces will have large effect in the displacement $x - x_0$. Figure 2.3 shows the relationship between trapping frequency and trapping stiffness:

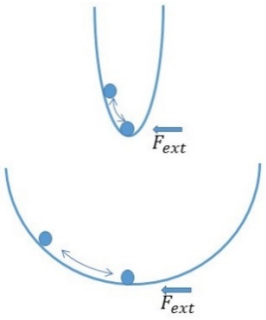

(Figure 2.3: Lowering of the optical trapping frequency results in a weaker trapping stiffness which gives rise to shallow potential. Hence, any small variation in external forces will result in a large response in displacement.)

Therefore, we need strong a gradient force along vertical direction to compensate gravitational and scattering force and a weak gradient force along transverse direction that amplifies the response due to an external force field.

2.4 Low Gradient Force with Non-Diffracting Beams

The basic challenge in this project is to come up with a scheme where we tailor an optical trapping beam with low but finite gradient force in a certain direction and keep the particle trapped. In this proposed setup, during initial trapping phase, a highly focused Gaussian beam along the vertical direction with strong scattering force will be used to trap the particle and compensate for gravity. But, we will also have strong gradient force along transverse directions which will trap the particle in the transverse plane. If we are to arbitrarily modulate the trapping force thus making the gradient force into arbitrary smaller value, the stiffness of the optical trap will also be weak; which means that we will have a weak gradient force and a weak confinement in the transverse plane. Thus, the particle will escape. Arbitrarily modulating the trapping force into smaller value will also result in a weak scattering force and gravity will force the particle out of the trap along the vertical direction. Apart from the above considerations, lowering the trapping force, hence lowering the scattering and dipole force, will make the Brownian motion of the particle in air forcing the particle out of the trap as well.

To overcome such obstacle and achieve lower but finite gradient force along a certain direction in the transverse (x, y) plane, we need to use two counter-propagating collimated beams along that certain direction. Collimated beams have transversal width (w_0) which is much larger than the wavelength (λ). If we consider the propagation distance for such a beam to be smaller than the diffraction length $x < x_R = 2\pi\, w_0^2/\lambda$, we will find that the gradient force along the propagation distance for the collimated beam is very small. The fundamental problem with such collimated beam is that, diffraction usually prevents transversely confined electromagnetic field to travel along the propagation direction with lower gradient. We can overcome such restriction by using special beams which have non-diffracting propagating properties over a long propagation distance such as Bessel-Gaussian beams.

The Bessel-Gaussian beam has a diffraction-free propagation over a long distance with negligible gradient forces along the propagation direction. If we use two counter-propagating Bessel-Gaussian beam, the scattering forces from the opposite directions can be cancelled out. The gradient force along the counter-propagating direction will be negligible. And, the gradient force along the transverse direction to propagation will confine the particle in the transverse plane. Now using two counter-propagating Bessel-Gaussian in the horizontal (x, y) plane in my setup, I will have negligible gradient force along the counter-propagation directions where the particle will become extremely sensitive to any external force. I will also have strong gradient force along vertical direction which will overcome gravitational force and keep the particle trapped in the vertical plane. Therefore, I will only need the focused Gaussian beam to initially trap the particle. I can then turn on the counter-propagating Bessel-Gaussian beams and gradually turn off the vertically trapping gaussian beam.

2.5 Bessel-Gaussian Beam

We have the well-known wave equation which is as follows:

$$\left(\nabla^2 - \frac{1}{c^2}\frac{\partial^2}{\partial t^2}\right)\varepsilon(r,t) = 0 \quad (2.38)$$

There are many solutions to the wave equation. One of the solution to the wave equation relies on Bessel function and hence called Bessel beam. The Bessel function solution to the wave equation results in beam profile that has a central core with surrounding concentric rings. An ideal Bessel beam is defined as follows (K. Dholakia et al, 2005):

$$E(r,\phi,z) = A_0 exp(ik_z z) J_n(k_r r) exp(\pm in\phi) \quad (2.39)$$

where $J_n$is the nth order Bessel function, $k_z$is longitudinal wave vector, k_r is the radial wave vector, $k = \sqrt{k_z^2 + k_r^2} = 2\pi/\lambda$, λ is wavelength of the electromagnetic radiation making up the

Bessel beam and r, ϕ and z are the radial, azimuthal and longitudinal respectively and $exp(\pm in\phi)$ is the azimuthal phase.

The zeroth order and higher order ($n > 0$) Bessel beam is shown in figure 2.4 respectively.

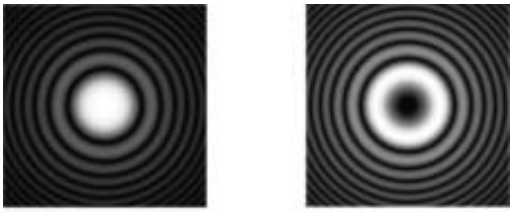

(a) (b)

(Figure 2.4: (a) Zero order Bessel beam transverse intensity profile (b) 1st order Bessel beam transverse intensity profile)

The higher order Bessel beams have phase singularity on the beam propagation axis and hence it has dark core.

The most notable feature of the Bessel beam is that this Bessel beam solution to the Helmholtz equation obeys the following relation (K. Dholakia et al, 2005, A. Stockham et al, 2006, J. Durnin, 1987):

$$I(x, y, z \geq 0) = I(x, y) \qquad (2.40)$$

This means that the time averaged intensity profile at $z = 0$ is reproduced at all $z > 0$ meaning that the cross-sectional plane normal to the propagation axis remains constant as the beam propagates. Therefore, the beam propagation can be considered as "Diffraction Free" propagation. The Bessel beam that I have addressed so far is an ideal form of Bessel beam which is not realizable physically. This is because, such ideal Bessel beam needs to contain an infinite number of rings over an infinitely large area and consequently carrying infinite amount of energy while propagating along an infinitely long distance. However, an approximation to the idealized Bessel beam can be made also known as quasi-Bessel beam. This quasi-Bessel beam will possess the properties of the Bessel beam over a finite distance z_{max}. It will have finite number of rings carrying finite amount of energy over finite extent. We will consider quasi-Bessel beam from now on.

There are numerous ways to generate quasi-Bessel beam. One of the most efficient way to generate quasi-Bessel beam is to use an incoming Gaussian beam incident on an Axicons generating Bessel-Gaussian beam as shown on figure 2.5:

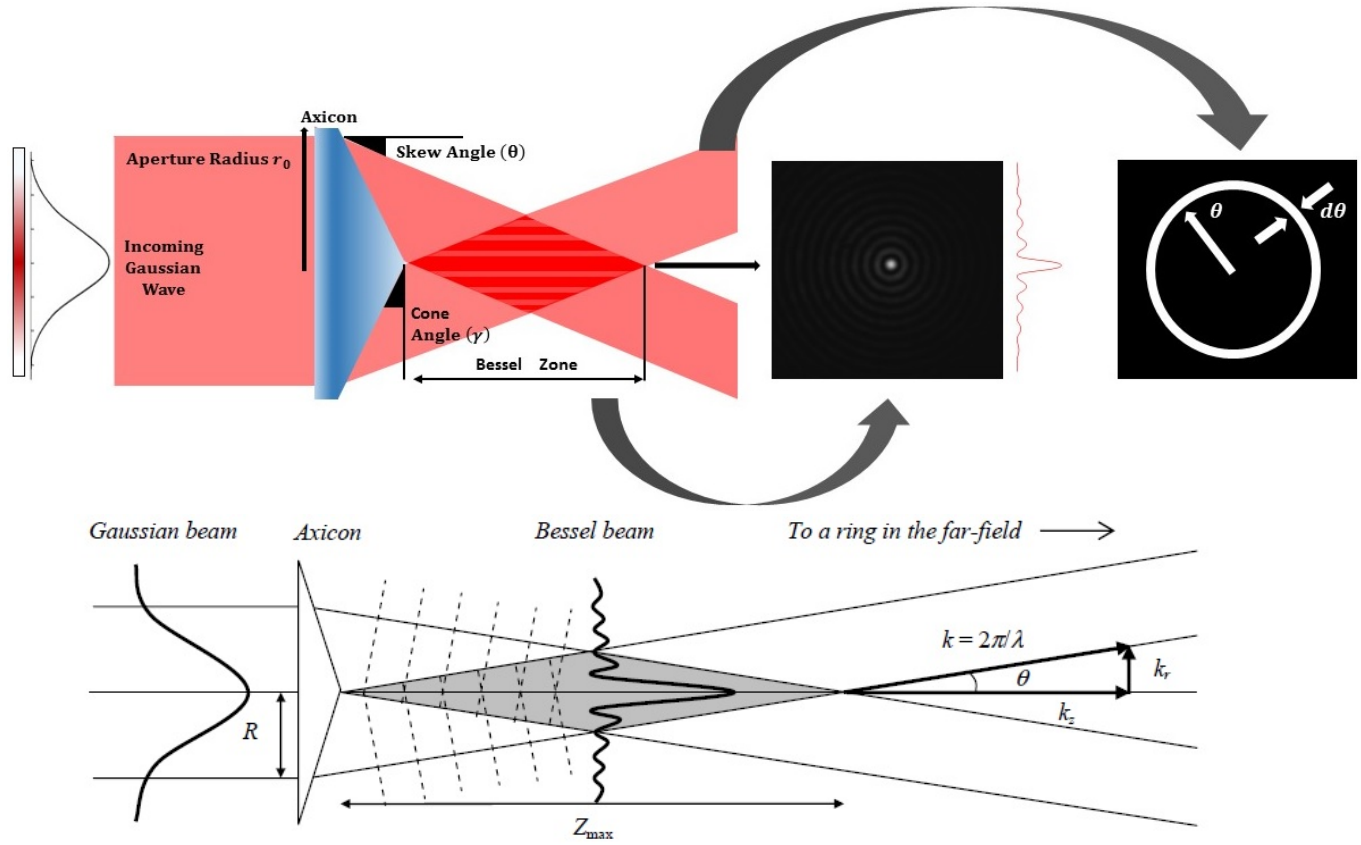

(Figure 2.5: (a) An axicon producing a Bessel beam when illuminated by an incoming Gaussian beam of radius *R*. The first inset shows the Bessel beam formed within the Bessel zone. The second inset shows the Fourier transform of the Bessel beam which is a ring in *k*-space. (b) The geometry of the creation of a Bessel-Gaussian beam using an axicon. The image is credited to A. Stockham et al, 2006.)

Now, the non-diffracting propagation does not imply that the Bessel beam is free from diffraction altogether. An alternate way of appreciating Bessel beam is to think of a set of plane waves propagating on a cone. Each of those propagating plane wave undergoes the same phase shift $k_z \Delta z$ over the distance of Δz. Such breakdown of the Bessel beam into constituent plane waves materializes itself in the angular spectrum which is a ring in the k-space or far-field per optical terminology. Refer to figure 2.5. This alternate mathematical appreciation of Bessel beam is nothing but an interference pattern formed by a set of coherent waves travelling on a cone in analogy with two-beam interference pattern. During the Bessel beam propagation, the energy in the outer rings diffract into the inner rings and vice versa. Given the energy in each ring is equal, the transverse intensity profile remains constant with propagation distance and the size of the central core remains fixed as a ratio of the wavelength to the cone angle (K. Dholakia et al, 2005, A. Stockham et al, 2006, J. Durnin, 1987).

While exhibiting such diffraction-free propagation, the Bessel beam is not well localized as Gaussian beam. Each of the surrounding concentric rings carries approximately the same energy as the central core and hence the more rings there are in the Bessel beam, the less energy in the central core.

The decomposition of the Bessel beam into constituent plane waves propagating on a cone gives us a mean to obtain the following characterizations of the Bessel beam (R. P. MacDonald et al, 1996, K. Dholakia et al, 2005, A. Stockham et al, 2006):

a) The opening angle of the cone along which the constituent plane waves travels:

$$\theta = \tan^{-1}\frac{k_r}{k_z} \approx \frac{k_r}{k_z} \text{ (small angle approximaton)} \qquad (2.41)$$

b) The opening cone angle can be used to define the radius of the central core of the Bessel beam:

$$r_0 = \frac{2.405}{k_r} \qquad (2.42)$$

c) The nodes of the beam correspond to a π phase shift between adjacent rings (Y. Lin et al, 1992, K. Dholakia et al, 2005).

Geometrically the maximum quasi-Bessel beam propagation distance, i.e. depth of field, is estimated by the following relation:

$$z_{max} = \frac{R}{\tan\theta} \approx \frac{R}{\theta} \text{ (small angle approximaton)} \qquad (2.43)$$

where R is the incoming gaussian beam radius. The opening angle of the cone is given by the following relation:

$$\theta = (n-1)\gamma \qquad (2.44)$$

where n is the refractive index of the axicon material and γ is the opening angle of the axicon. Therefore, it is also possible to show that for axicon generated quasi-Bessel beam, the following relations holds true:

$$z_{max} = \frac{R}{\theta} = \frac{R}{(n-1)\gamma} \qquad (2.45)$$

In this project, we will consider generating quasi-Bessel beam such as Bessel-Gaussian beam using Axicons and Spatial Light Modulator(SLM). SLMs are discussed later in section 2.6. Now considering the Bessel beam as a set of plane waves propagating on a cone reveals yet another amazing property; that is self-reconstruction property. If an obstruction is placed in the beam propagation path, the plane wave fronts propagating along the surface of a cone will diffract around the cone and will cast a shadow into the beam but eventually reforming the intensity Bessel profile beyond the obstruction point (R. M. Herman et al, 1991, K. Dholakia et al, 2005, A. Stockham et al, 2006). See section 2.6.4 for experimental realization of this self-reconstructing property of quasi-Bessel beam.

Finally, there are few other important properties of the quasi-Bessel beam to consider. The first one to note is has a large depth of field (z_{max}). If we define the range of a Gaussian beam as some distance z at which the Gaussian beam's intensity fall by a factor of two, it happens to be the following:

$$\text{Quasi Bessel beam depth of field} \approx N \times \text{Gaussian beam depth of field} \quad (2.46)$$

where N is the total number of rings in the quasi-Bessel beam. In order to have a comparison between the two types beam, it is assumed in this writing that the waist of the Gaussian beam is equal in size to the central core of the Bessel beam. The central core can be extremely small making it very intense. However, the energy in each ring is equal and as a result we have the following relation (A. Stockham et al, 2006, F. Gori, 1987, J. Durnin et al, 1988):

$$\text{Power in central core of quasi Bessel beam} \approx \text{total Gaussian power} \div N \quad (2.47)$$

Also, the total number of rings N in the Bessel function can be written as:

$$N = \frac{R}{2r_0} \qquad (2.48)$$

In this chapter, I have discussed few notable properties of quasi-Bessel beams such as diffraction-less propagation for a finite distance and self-healing properties. I have also shown how to calculate the depth of field, the central core radius and the number of rings of quasi-Bessel beams. In the next chapter, I present a small experiment to study the self-healing property of quasi-Bessel beam.

2.6 Self-reconstructing property of the Bessel Beam generated by a Spatial Light Modulator (SLM)

2.6.1 Creation of Single Bessel Beam

In this small initial exercise, I study the reconstructing property of the Bessel beam. Spatial Light Modulator (SLM) was used to generate a Bessel beam by mimicking directly a glass axicon. The Bessel beam generated by SLM will travel diffraction free for a given distance (Bessel zone) and will start to diffract again. I also show the evolution central core radius and the average central core intensity of the Bessel-Gaussian beam as the beam start to diffract.

The use of diffraction gratings to shape light beam to any desired pattern is called "Diffractive Optics" or "Computer Generated Lithography". The use of diffractive optics to shape laser beam dates several decades back but it was not until the last decade that a reconfigurable technology of generating arbitrary shaped beam was developed and advanced. This

reconfigurable technology is called Spatial Light Modulator (SLM) which allows arbitrary phase pattern to be applied to the laser beam. SLMs are essentially computer-generated holograms.

SLMs are made of thin liquid crystal cells and light beams are projected onto those crystal cells. When voltage is applied across the cells, a phase delay can be introduced in the reflected light beam from those crystal cells. The application of same electric field and consequently the same phase across the entire cell aperture will preserve the beam shape upon reflection. To generate a desired phase structure, an electric field with varying strength across the cell aperture is applied and consequently it will change the phase of the reflected light beam such that during propagation the intensity and phase cross-section of the beam transforms into desired pattern. In most common industry application, the liquid cells are attached to a programmable, pixelated CMOS array to create any desired spatially varying electric field. The entire device is used in reflection mode essentially doubling the available phase shift. Each pixelated CMOS in the SLM can generate a full 2π phase shift with video resolution and update rates. These programmable SLMs are programmed to be used as a secondary monitor and attached to the computer via graphics card such that an 8-bit greyscale image gives 256 different phase levels. Therefore, SLMs are essentially playing the role of a complicated diffraction gratings (R. Bowman et al, 2011).

SLM can be used in the image plane of the system and converting phase into intensity modulation with generalized phase construct (R. Bowman et al, 2011, P. Rodrigo et al, 2005,). SLM can also be used to project desired shapes close to the SLM in a Fresnel plane (A. Jesacher et al, 2004, R. Bowman et al, 2011). For this project, Fresnel plane is considered where a SLM is used to mimic an axicon thus producing a Bessel beam right after the plane of the SLM.

2.6.2 Creation of Single Bessel Beam

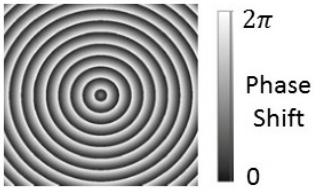

(Figure 2.6: The hologram computed in LabVIEW using the phase profile of an axicon)

A single Bessel beam is generated by mimicking a 7° axicon on the SLM using the hologram as shown in figure 2.6. The hologram in figure 2.6 was computed in LabVIEW visual programming software using the phase profile of an axicon:

$$e^{ik\theta r} \qquad (2.49)$$

where $k = 2\pi/\lambda$ is the wavenumber, r is the radial distance from the center of the axicon to the respective pixel and θ is the angle between rays of Bessel beam and optical axis. θ is related to

the cone angle γ of the axicon by the following relation: $\theta = (n_{ax} - 1)\gamma$ where n_{ax} is the refractive index of the axicon.

2.6.3 Experimental Setup

The experimental setup for single Bessel beam generation is shown in figure 2.7. The SLM used for this experiment is Cambridge Correlators SDE1024 phase only modulator. It has a resolution of 1024×768 pixel, bit-depth of $8 - bit$ and a pixel pitch of $9 \times 9\ \mu m$. Two lenses of focal length of $f_1 = 50mm$ and $f_2 = 50mm$ was used to image the SLM plane mimicking axicon onto a CCD camera. The CCD camera was translated along the propagation direction so that the evolution and propagation of the Bessel beam could be monitored. Next, a thin razor blade was also mounted on a 1D translation stage and the sharp edge of the blade was positioned such that it could be moved transversely to the propagation direction of the Bessel beam. The blade was stationed in the Bessel zone, merely touching the edge of the Bessel beam, 1cm before the CCD camera. The blade was gradually moved along transverse direction cutting the beam along the transverse plane. The reconstructive property of the Bessel beam was monitored on the CCD camera. The Bessel beam generated by the SLM in this project is of $\sim 4mm$ in diameter.

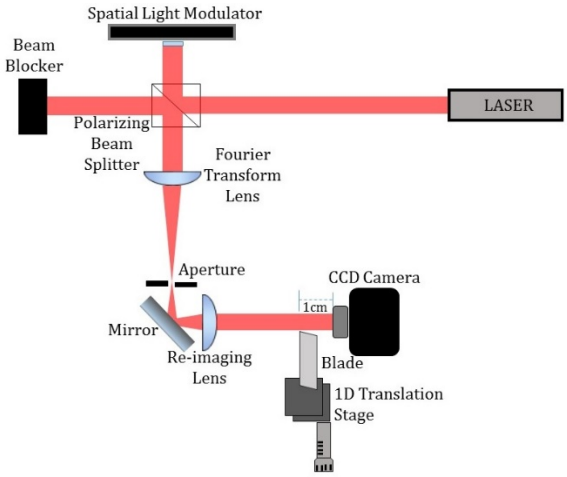

(Figure 2.7: The schematic representation of the setup of the Bessel beam generation using a SLM. A laser diode is used to generate laser beam. A polarizing beam splitter (PBS) is used to split the beam in half. The first half of the beam passing straight through the PBS is blocked by a beam blocker. The second half of the beam is incident on the whole of SLM pixel-array plane. The phase profile of Bessel beam is applied immediately after the SLM plane and the reflected beam picks up the Bessel beam profile while propagating. Next, the Fourier transform lens takes the reflected beam into Fourier plane where tiny rings are formed. The first order ring is selected by the aperture and reflected through a mirror onto the re-imaging lens. The re-imaging lens reconstructs the Bessel beam in image plane where the CCD camera is positioned. Far beyond the CCD camera we have Fourier plane (Fraunhofer – far field) where thin circular ring is formed in *k*-space. A razor thin blade is mounted on a 1D translation stage 1cm before the CCD camera.)

2.6.4 Results

Figure 2.8 shows an array of 3 × 3 Bessel beam images. In this small exercise, the diffraction free Bessel zone was not imaged which I will consider rigorously in chapter 3. The images were captured when the Bessel beam started to diffract. An arbitrary position close to the end of Bessel zone was taken to be a zero position and the images were recorded at 30mm, 60mm, 90mm, 120mm, 150mm and 180mm from the zero position. It also shows the fitting of the Bessel beam generated by SLM with a Bessel function of first kind function using MATLAB and the FWHM of the central core for each Bessel beam images was extracted.

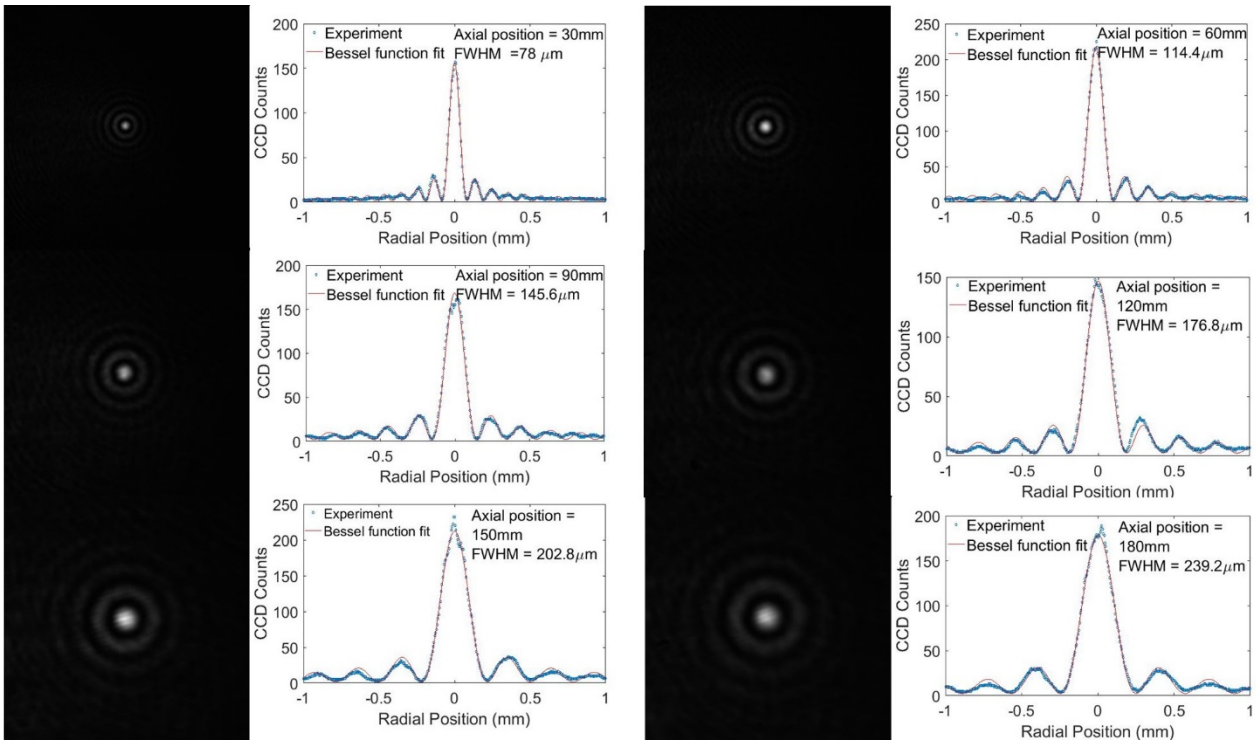

(Figure 2.8: An array of 3 × 3 Bessel beam images were recorded at 30mm, 60mm, 90mm, 120, 150mm and 180mm from an arbitrary zero position chosen close to the beginning point of Bessel zone. Each of the Bessel beam images were fitted with a Bessel function of first kind function using MATLAB and the FWHM of the central core for each of the Bessel beam images was extracted.)

The sequence of images shows that the Bessel beam is diffracting and the central core is gradually increasing. Next, figure 2.9 shows the percentage of power of the central core of Bessel beam recorded at position mentioned in figure 2.8. The average power of the central core of the Bessel beam is ~5% of the total beam intensity.

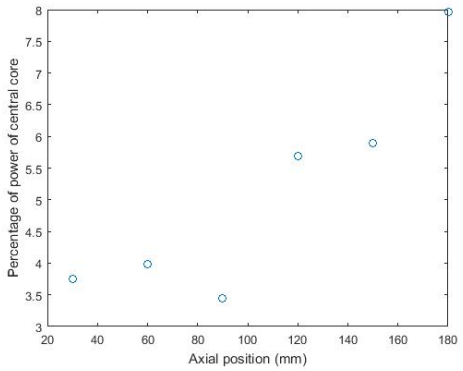

(Figure 2.9: The percentage of power of the central core of Bessel beam recorded at the position of 30mm, 60mm, 90mm, 120, 150mm within the Bessel zone.)

Finally, figure 2.10 shows an array of 3 × 2 Bessel beam images recorded as the blade was gradually translated along transverse plane of the beam propagation axis. The first image is when the blade is merely touching the edge of the beam, next image is when the blade is moved 2mm transversely inside the beam, then 2.2mm inside, then 2.3 mm inside, 2.4 mm and finally 3.0 mm inside the Bessel beam. We can see the reconstruction property of the Bessel beam even after the central core was completely obstructed.

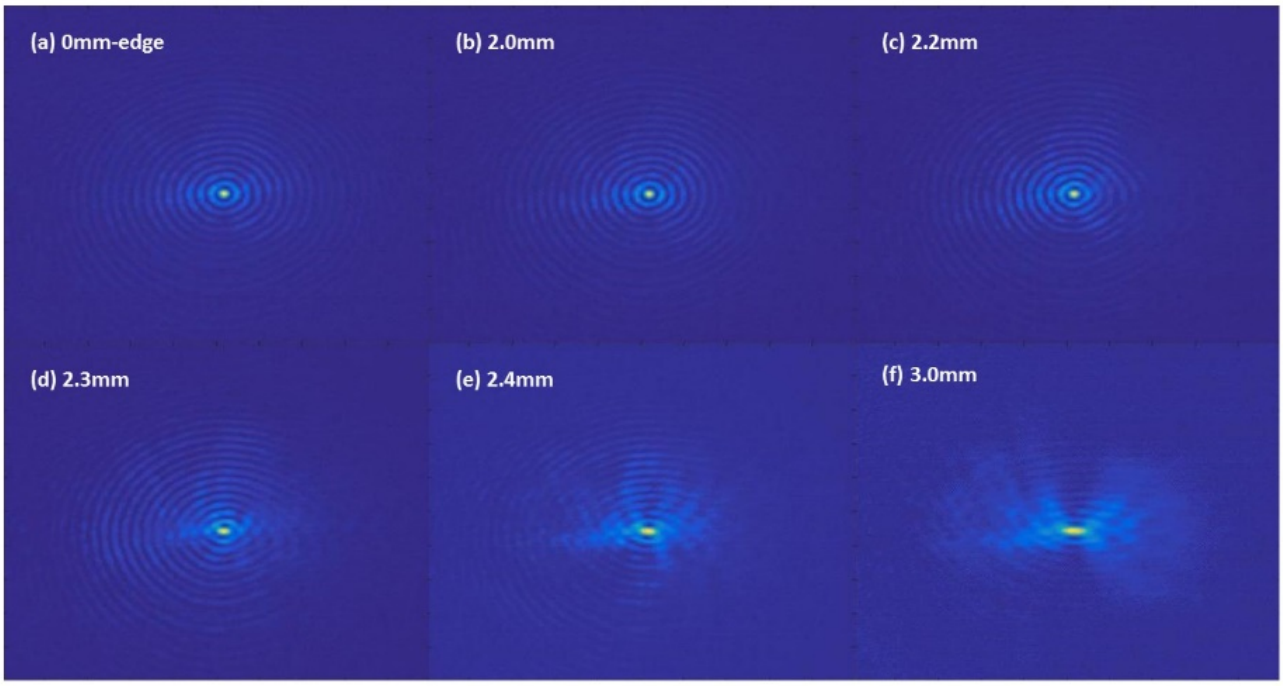

(Figure 2.10: An array of 3 × 2 Bessel beam images recorded as the blade was gradually translated along transverse plane of the beam propagation axis. The images show the amazing re-constructing property of the Bessel beam.)

2.6.5 Conclusions

Although more rigorous measurement techniques were needed to further precisely measure the central core intensity and the reconstruction property of the Bessel beam, the core objective of this small additional experiment was to investigate and derive an overall ballpark

appreciation of the reconstruction property of the Bessel beam. In the next chapter, I address some inherent challenges of implementing optical trapping with Bessel-Gaussian beam that I need to overcome.

2.7 Trapping with Bessel-Gaussian Beam – Possibilities and Challenges

In this chapter, I present a brief qualitative study of the possibilities and challenges of trapping with counter-propagating Bessel-Gaussian beam in my setup. The implementation of my experimental setup is addressed in detail in chapter 4. A 1650mW laser (1064nm wavelength) is used in my setup and I have directed 85% (1450mW) of the total laser power towards the two axicons to create two counter-propagating Bessel-Gaussian beams. 1450mW is split into two equal halves using beam splitter, leaving 725mW incident on each axicon. I have a shallow 5° axicon pair and a sharp 20° axicon pair and an incoming Gaussian beam radius of 1.5mm. I present the calculation of maximum propagation distance (Bessel zone), central core diameter, Number of rings and central core intensity of Bessel-Gaussian beam generated by both pairs of axicons and qualitatively appreciate the feasibility of optical trapping (table 2.1).

Characteristics of Bessel-Gaussian Beam (R=1.5mm)	$\gamma = 5^{\circ}$	$\gamma = 20^{\circ}$
Opening angle of the cone: $\theta = (n-1)\gamma$	0.0393	0.157
Depth of field: z_{max} (mm)	38.197	9.55
Central core radius: r_0 (mm)	0.0104	0.0026
Number of rings: N	72.3	288.082
Central core intensity: I_{core} (mW)	10.0278	2.5166

(Table 2.1: Various Bessel-Gaussian beam parameters generated by 5° and 20° axicons)

From table 2.1, we can see that using 5° axicon produces a long propagation distance of ~38mm with ~10mW central core power and small number of rings. Using two counter-propagating beams, we have ~20mW of total power. The significant drawback is that it produces ~20μ diameter central core. Such a large focal waist will produce very small gradient force making it unsuitable for trapping. Also, with the benefit of hindsight, the total central Bessel core power of ~20mW is not sufficient for optical trapping. Therefore, my natural intuition was to deploy a very sharp angle axicon to produce a very tight focal waist which will produce significantly large gradient force. We can see from table 2.1 that using a 20° axicon, with the same the incoming Gaussian beam diameter, will produce a central core diameter of ~5.2μ which is still significantly large. The depth of field ~9.5mm is significantly large enough. The drawback is that, the 20° axicon produces significantly many rings which in turn reduces the central core intensity of the beam to ~2.5mW. The two counter-propagating beams will give merely ~5mW of total power. I opted for the sharpest 20° axicon since it will produce comparatively smaller

central core focal waist. Now, I need to find a solution for generating Bessel-Gaussian beam with relatively tight focal point, longer propagation distances and higher central core intensity.
In the next chapter, I present a simple and compact design for generating quasi Bessel-Gaussian, i.e. Bessel-like, beam with relatively tight foci, high central core power and long effective propagation distance which.

Chapter 3

Spatial Characterization Bessel-Gaussian Beam: Lens-Axicon System

3.1 Abstract

In this study, I present a simple and compact design for generating and manipulating the spot size and effective focal length of the Bessel-Gaussian, i.e. Bessel-like, beams. I have studied the possibility of focusing the Bessel-Gaussian modes to reduced focal spot sizes as well as maintaining an effective longer focal length with increased central core beam intensity using both a sharp and shallow axicon in combination with a spherical lens. A theoretical calculation of the spatial characterization of the resulting focal profiles of the lens-axicon system is carried out and the experimental measurement is obtained in detail using an accurate high dynamic range imaging technique. This setup overcomes the typical compromise between small spot size and an effective long propagating distance of Bessel-Gaussian beams. This is particularly promising for optical trapping with Bessel-Gaussian beams as it provides an effective solution to optical trapping using two counter-propagating Bessel-Gaussian beams where a compromise is no longer required for obtaining a small central core spot size with the cost of having a shorter propagation distance.

3.2 Introduction

Diffraction is the foundational property of optical physics and has an undeniable presence in the design of all forms of optical systems (K. Dholakia, 2005, S. Akturk, 2012). Diffraction is the inevitable result of the wave nature of light and this phenomenon manifests when electromagnetic waves encounters any finite apertures. Diffraction plays the following few significant defining roles in the focusing of Gaussian beam i.e. laser beam. Firstly, the smallest spot size of the focused Gaussian beam is limited by the laser wavelength also known as diffraction limit. Secondly, the Gaussian beam stays focused within a propagation length known as the Rayleigh range which is proportional to the square of the beam waist. And finally, the

Rayleigh range determines the depth of focus i.e. the region where the beam intensity stays high (K. Dholakia, 2005, Ming Lei et al. 2004, S. Akturk, 2012). Even though the laser beam is deemed to have low divergence, nevertheless it is subject to diffraction which causes the beam to spread. The tighter a Gaussian beam is focused, the more rapidly the beam diverges. Such restriction makes single-beam optical trapping, i.e. Optical Tweezers, only effective near the focal region.

The use of Bessel-Gaussian beams by an axicon to exceed the Rayleigh range while maintaining the same spot size as of the focused Gaussian beam has drawn interest in optical trapping (C. A. McQueen et al, 1999, J. Arlt et al, 2000, J. Arlt et al, 2001, Karen Volke-Sepúlveda et al, 2004, S. Monk et al, 1999). The most desirable property of Bessel-Gaussian beam over a typical Gaussian beam is the ability to overcome the limitations of the Rayleigh range (Adam M. Summers et al, 2017, Ming Lei et al. 2004, R. Grunwald et al, 2004, V. Jarutis et al, 2000) while maintaining the same spot size propagation and on-axis peak intensity for much longer distance, i.e. Bessel zone, without any beam spreading due to diffraction.

There are few notable ways of generating Bessel-Gaussian beams including Diffractive Optics, Spatial Light Modulators (SLM) and Axicons amongst which SLMs and Axicons are most prominent. There is a tradeoff between choosing Axicons or SLMs. Axicons are most widely used for generating Bessel-Gaussian beams. The advantage of using an SLM over an Axicon is the great degree of control that an SLM provides. However, SLMs can be complicated and expensive to implement. SLMs also have fairly low peak power and average power damage thresholds and renders it usable only with moderate pulse energies and repetition rates. Whereas, Axicons are easy to implement and have low energy loss (Adam M. Summers et al, 2017). By controlling the apex angle or the sharpness of an Axicon and the input Gaussian beam diameter, it is possible to tailor the focal beam profile of the Bessel-Gaussian beam to meet the specific needs of the Optical Trapping setup.

However, even before Bessel-Gaussian beams can be used for optical trapping, there is a significant challenge that needs to be addressed; which is to overcome the typical compromise between small spot size and an effective long propagating distance, i.e. Bessel zone, of Bessel-Gaussian beams. A sharp Axicon or large apex angle Axicon produces a central core beam with smaller spot size, i.e. tight foci, and higher intensity focal region. But the diffraction-free propagation distance or effective focal length becomes very short. By increasing the incoming Gaussian beam diameter, it is possible to increase the Bessel zone. However, the concentric rings also increase significantly resulting in lower intensity in the central core of the beam since power is distributed equally amongst the central core and each concentric ring. To overcome

such hurdle, a shallow Axicon or low small apex angle axicon can be used to produce longer focal length or Bessel zone and sending incoming Gaussian beam with smaller diameter, it is possible to increase the central core intensity. Yet again, using shallow Axicons produces a very large spot size or large focal waist which in turn limits the maximum achievable central core gradient to lower values and very small gradient force. Therefore, a compromise needs to be made, when using Bessel-Gaussian beam for optical trapping, between tight focal point and longer propagation distances.

In this study, I present a simple and compact design for generating quasi Bessel-Gaussian, i.e. Bessel-like, beam with relatively tight foci and long effective propagation distance. The placement of a positive spherical lens before an axicon of shallow apex angle and tailoring the incoming Gaussian beam width, it is possible to produce tight focal spot sizes while keeping the effective propagation distances long enough to make optical trapping possible with counter propagating Bessel-Gaussian beams.

3.3 Theory

The theoretical model for the lens-axicon system is developed from the scaler Kirchhoff theory of diffraction. The three-dimensional (Fresnel) wave distribution emanating from a circular aperture near the focus can be evaluated from the Debye integral resulting in the usual Kirchhoff-Fresnel integral (M. Rorn et al, 1975). The model for the lens-axicon system is derived in two-step process. We begin the first step with an incoming collimated Gaussian beam which is incident on the lens. The beam is then propagated through the lens, adding the phase factor, by distance *d* using Kirchhoff-Fresnel integral. The cylindrically symmetric intensity profile at distance *d* (axicon plane) from the lens and at distance r_1 from the optical axis can be written as:

$$u(\rho_1, d) = \int_0^{a_1} A(\rho_1) e^{-ik\frac{\rho_1^2}{2d}} J_0\left(\frac{kr_1\rho_1}{d}\right) \rho_1 \, d\rho_1 \qquad (3.1)$$

where $k = 2\pi/\lambda$ is the wavenumber for the light of wavelength λ and J_0 is the Bessel function of zero order. Next, we begin the second step by performing another Kirchhoff-Fresnel integral to propagate the beam profile calculated at the axicon plane through the axicon adding the axicon phase factor. Finally, the resultant cylindrically symmetric intensity profile from the tip of the axicon along the axial distance and at distance r_2 from the optical axis can be written as:

$$u(\rho_2, z) = \frac{k}{z} \int_0^{a_2} u(\rho_1, d)\, A(\rho_2) e^{-ik\frac{\rho_2^2}{2z}} J_0\left(\frac{kr_2\rho_2}{z}\right) \rho_2 d\rho_2 \quad (3.2)$$

Below is the schematics of the propagation of collimated Gaussian beam through lens-axicon system.

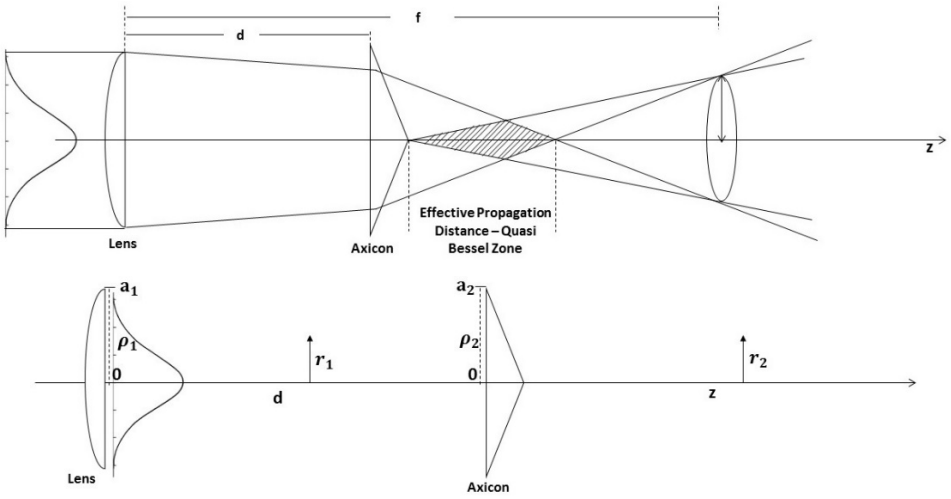

(Figure 3.1: (a) Schematic of optical arrangement for converging lens-axicon system. (b) Start with a collimated Gaussian beam incident on the lens. The beam is then propagated through the lens, adding the phase factor, by distance d and integrated over ρ_1 using Kirchhoff-Fresnel integral. Then, we have a cylindrically symmetric intensity profile at distance d (axicon plane) from the lens and at a distance r_1 from the optical axis. Next, another Kirchhoff-Fresnel integral over ρ_2 is performed to propagate the beam profile calculated at the axicon plane through the axicon adding the axicon phase factor. Finally, we have a cylindrically symmetric intensity profile from the tip of the axicon along the axial distance and at distance r_2 from the optical axis)

Consider a laser beam illuminating a lens and the amplitude distribution at the lens can be written as

$$A(\rho_1) = A(\rho_1)_{beam} A(\rho_1)_{lens} \qquad (3.3)$$

where $A(\rho_1)_{beam}$ is the input beam distribution and $A(\rho_1)_{lens}$ is the phase retardation due to lens.

The collimated Gaussian input amplitude distribution is given by (A. E. Siegman, 1986)

$$A(\rho_1)_{beam} = \sqrt{I_0} e^{-\left(\frac{\rho_1}{W}\right)^2} \qquad (3.4)$$

where W is the beam waist at the lens and I_0 is the on-axis intensity for a large radius of curvature spherical wave. The phase retardation factor of a thin lens is calculated from the varying thickness of the lens and given by (A. Nussbaum et al, 1976)

$$A(\rho_1)_{lens} = e^{-ik(n_{lens}-1)\left\{R_1\left[1-\sqrt{1-\frac{\rho_1^2}{R_1^2}}\right]-R_2\left[1-\sqrt{1-\frac{\rho_1^2}{R_2^2}}\right]\right\}} \qquad (3.5)$$

$$\approx e^{-ik(n_{lens}-1)\left\{R_1\left[1-\sqrt{1-\frac{\rho_1^2}{R_1^2}}\right]\right\}} \qquad (3.6)$$

where n_{lens} is the refractive index of lens, R_1 and R_2 are the radii of curvature. For plano-convex lens, $R_2 \to \infty$. Therefore, we can neglect the R_2 term in the equation. The equation includes the effects of spherical aberrations.

Therefore, using the usual Kirchhoff-Fresnel integral, the intensity profile on the other side of the lens with is given by

$$u(\rho_1, d) = \int_0^{a_1} \sqrt{I_0} e^{-\left(\frac{\rho_1}{W}\right)^2} e^{-ik(n_{lens}-1)\left\{R_1\left[1-\sqrt{1-\frac{\rho_1^2}{R_1^2}}\right]\right\}} e^{-ik\frac{\rho_1^2}{2d}} J_0\left(\frac{kr_1\rho_1}{d}\right)\rho_1\, d\rho_1 \quad (3.7)$$

Here the Gaussian beam passes through the focusing lens and propagates trough a distance d and finally incident upon the axicon plane. Next, we use the Kirchhoff-Fresnel integral again and add the phase retardation due to axicon which is given by

$$e^{-ik(n_{axicon}-1)\propto_{axicon}\rho_2} \quad (3.8)$$

where n_{axicon} is refractive index of the axicon and $\propto_{axicon}$ is the apex angle of the axicon (tan $\propto_{axicon} \cong \propto_{axicon}$ small angle approximation).

Finally, the exact analytical solution for the intensity profile or cylindrically symmetric amplitude distribution at distance z from the lens-axicon system and at distance ρ_2 from the optical axis can be written using the usual Kirchhoff-Fresnel integral:

$$u(\rho_2, z) =$$

$$\frac{k}{z}\int_0^{a_2}\int_0^{a_1} \sqrt{I_0} e^{-\left(\frac{\rho_1}{W}\right)^2} e^{-ik(n_{lens}-1)\left\{R_1\left[1-\sqrt{1-\frac{\rho_1^2}{R_1^2}}\right]\right\}} e^{-ik\frac{\rho_1^2}{2d}} J_0\left(\frac{kr_1\rho_1}{d}\right)\rho_1\, d\rho_1 e^{-ik(n-1)\propto\rho_2} e^{-ik\frac{\rho_2^2}{2z}} J_0\left(\frac{kr_2\rho_2}{z}\right)\rho_2 d\rho_2 \quad (3.9)$$

Numerically solving the above double integral equation is extremely difficult. Further simplifications are required.

An alternative simplified method of calculating the intensity profile for the lens-axicon system using Gaussian optics is presented for this work. In this method, we will replace the first Kirchhoff-Fresnel integral with Gaussian optics and then add the phase retardation due to the axicon and finally invoking the usual Kirchhoff-Fresnel integral. This way we can reduce the double integral in the above equation to one integral and numerically solve it. The exact analytical solution with two Kirchhoff-Fresnel integrals, used radius of curvatures in lens phase retardation term. This was an exact replication of spherical lenses and will include spherical aberrations. Whereas, replacing the first integral with Gaussian optics assumes aberration free parabolic lenses and will not include spherical aberrations.

Therefore, the redefined cylindrically symmetric intensity profile from the tip of the axicon along the axial distance and at distance r from the optical axis can be written as:

$$U(\rho, z) = \frac{k}{z}\int_0^a \frac{W}{W(z)} e^{-\frac{\rho^2}{W^2(z)}} e^{-ik\left[\frac{\rho^2}{2R(z)}-(n-1)\alpha\rho\right]} e^{-i[kz-\phi z]} e^{-ik\frac{\rho^2}{2z}} J_0\left(\frac{kr\rho}{z}\right)\rho\, d\rho \quad (3.10)$$

Let us begin with the general form of normalized Gaussian beam after propagating from origin to a position z represented by the beam waist W_0 and Rayleigh length z_R:

$$\frac{E(x,y,z)}{E_0} = \frac{W_0}{W(z)} e^{-\frac{\rho^2}{W^2(z)}} e^{-i\frac{k\rho^2}{2R(z)}} e^{-i[kz-\emptyset(z)]} \quad (3.11)$$

Gaussian beam spot size:

$$W(z) = W_0\sqrt{1+\left(\frac{z}{z_R}\right)^2} \quad (3.12)$$

Radius of curvature:

$$R(z) = z\left[1+\left(\frac{z_R}{z}\right)^2\right] \quad (3.13)$$

Guoy phase shift:

$$\emptyset(z) = \tan^{-1}\frac{z}{z_R} \quad (3.14)$$

W_0 and z_R are related by, $z_R = \frac{\pi n W_0^2}{\lambda_0}$ which gives the value for beam waist:

$$W_0 = \sqrt{\frac{z_R\lambda_0}{\pi n}} \quad (3.15)$$

The spot size can be further simplified as (figure 3.2):

$$W(z) \cong W_0\left(\frac{z}{z_R}\right) \text{ when } z \gg z_R \quad (3.16)$$

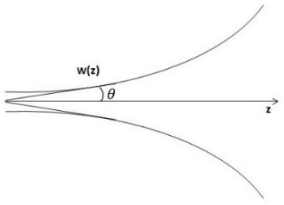

(Figure 3.2: Beam spreading angle for $z \gg z_R$)

Hence the relation between $W(z)$ and z becomes linear and the beam spreading angle is defined as:

$$\frac{W(z)}{z} = \frac{W_0}{z_R} = \frac{W_0}{n\pi W_0^2/\lambda_0} = \frac{\lambda_0}{n\pi W_0} = \tan\theta \quad (3.17)$$

Now from the geometry of the lens (figure 3.3) we get:

$$\tan\theta = \frac{W}{f} \quad (3.18)$$

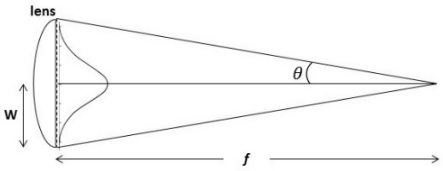

(Figure 3.3: Geometry for focusing of convex lens)

From equations 3.17 and 3.18:

$$\frac{W}{f} = \frac{\lambda_0}{n\pi W_0} \quad (3.19)$$

$$\therefore W_0 = \frac{\lambda_0 f}{n\pi W} \qquad (3.20)$$

From equations 3.15 and 3.20:

$$\sqrt{\frac{z_R \lambda_0}{\pi n}} = \frac{\lambda_0 f}{n\pi W} \qquad (3.21)$$

$$\therefore z_R = \frac{\lambda_0 f^2}{n\pi W^2} \qquad (3.22)$$

Now we have W_0 and z_R redefined in terms of lens aperture radius. To find the Gaussian beam propagation at axicon aperture, we use *z=d-f* and use the redefined equations 3.20 and 3.22 into equation 3.12, 3.13 and 3.14. Finally invoking the usual Kirchhoff-Fresnel integral and adding the phase retardation due to axicon:

$$U(\rho, z) = \frac{k}{z}\int_0^a \frac{W}{W(d-f)} e^{-\frac{\rho^2}{W^2(d-f)}} e^{-ik\left[\frac{\rho^2}{2R(d-f)} - (n-1)\alpha\rho\right]} e^{-i[k(d-f)-\phi(d-f)]} e^{-ik\frac{\rho^2}{2z}} J_0\left(\frac{kr\rho}{z}\right)\rho\, d\rho \quad (3.23)$$

Figure shows the schematics of the geometry of the lens-axicon system using Gaussian optics:

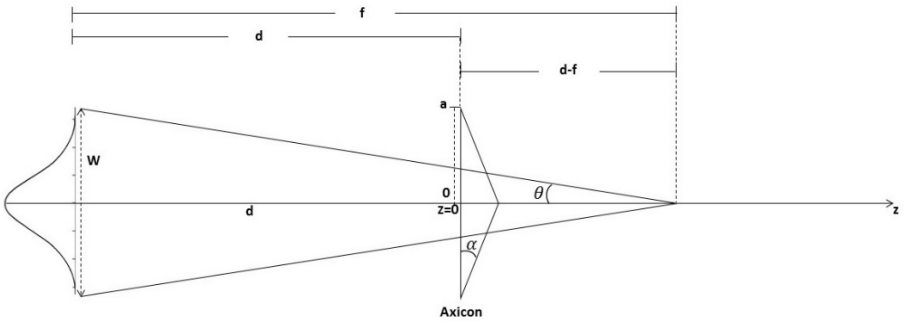

(Figure 3.4: Schematic of optical arrangement for converging lens-axicon system using Gaussian optics)

3.4 Experimental Setup

A schematic of the setup is shown in figure 3.5. An image of the experimental setup is also shown in figure 3.6. I have used a 532nm diode laser (CPS532, Thorlabs). The laser is fiber coupled and directed through a half wave plate, a quarter wave plate and polarizer. The beam is then incident on a spherical lens and then the focused Gaussian beam is incident on an Axicon. Both the spherical lens and Axicon is mounted on a 1D translation stage. The beam produced from the tip of the Axicon is quasi Bessel-Gaussian beam. An imaging lens is placed within the proximity of the Bessel zone or effective propagation distance to produce magnified images of the Bessel zone. A CCD camera (DCC1545M, Thorlabs) is placed at a distance to give 52 times magnification of the image plane. The 1D translation stage is moved to scan through the entire Bessel zone. A positive spherical Plano convex lens with focal lengths of 30mm or 50mm was placed in front of UV fused Silica Axicon (Thorlabs) with an apex angle of 5° or 20°. Both lenses and Axicons are $1^{"}$ or 25.4mm in diameter. The distance between the lens and the Axicon is changed to fine tune the focal spot size and the axial depth of field or Bessel zone of the quasi Bessel-Gaussian beam.

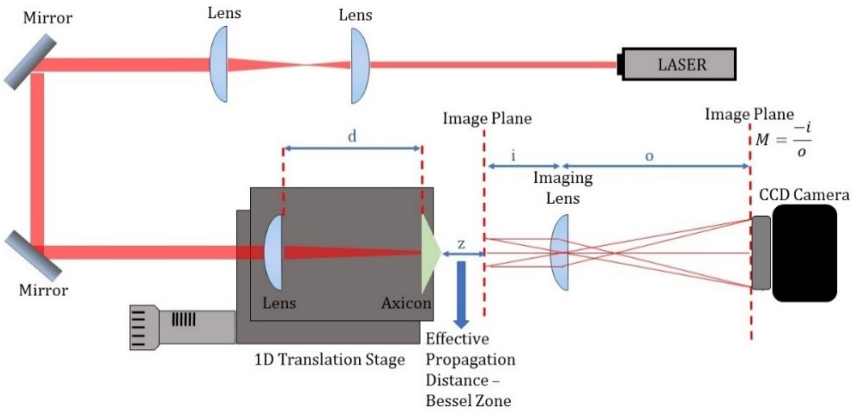

(Figure 3.5: Schematics of the experimental setup for lens-axicon system)

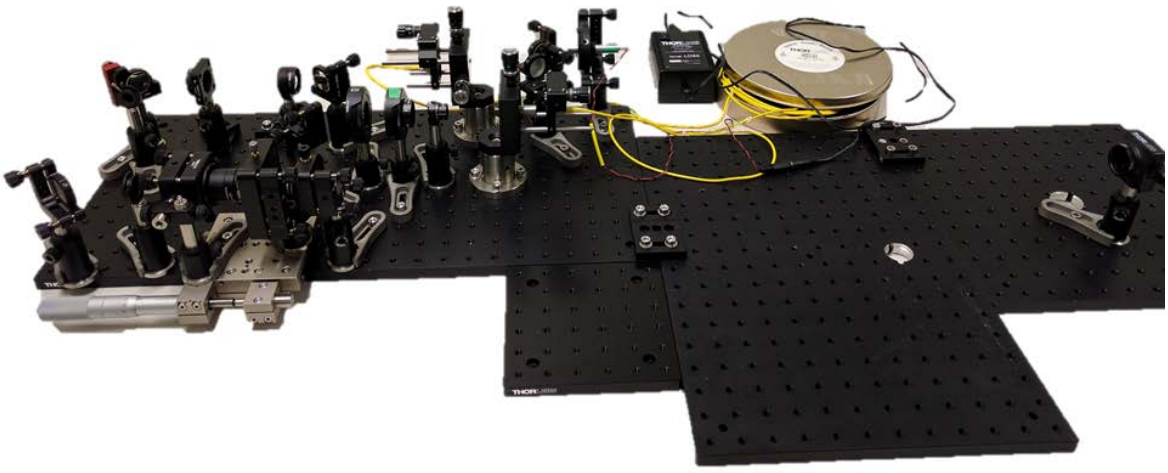

(Figure 3.6: Real image of the experimental setup for lens-axicon system)

The correct determination of intensity distribution becomes extremely difficult for beams with large variation in optical intensity. The Bessel-Gaussian beam is one such example. In Bessel-like beams, the intensity of each ring falls off monotonically as a function of radius since the core and each of the outer rings contains the same amount of energy (A. Stockham et al, 2006, F. Gori, 1987, J. Durnin et al, 1988). Now to have accurate focal profile analysis, a high bit depth imaging technique is required to capture the concentric rings and the minima in between the rings. The camera utilized in this work is 8 bits bit depth and hence I have used high dynamic range (HDR) imaging technique to extend the bit-depth of the camera. This way I could perform detailed and accurate measurements of beam profile without the need for expensive high bit depth CCD cameras.

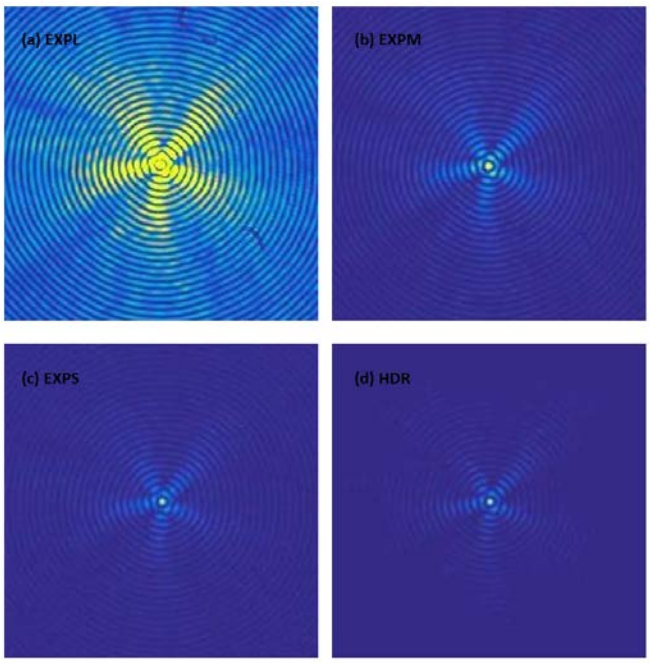

(Figure 3.7: An example of HDR image processing. Images (a), (b) and (c) are obtained with three different exposure times. A combined HDR image is shown in (d))

Three distinct images with different exposure times (long, medium and short) were captured at each axial (z – Bessel zone) positions. Exposure times were varied such as to make high intensity region saturated as shown in figure 3.7(a) and to make the low intensity region nearly invisible as shown in figure 3.7(c). Then, I have written an algorithm in MATLAB that takes those three images with different exposure times and then merged them together and a final HDR image is generated. This is done by replacing the saturated pixels of the image with medium exposure time (EXPM) with the corresponding pixels of the image with short exposure time (EXPS) and then the saturated pixels of the image with long exposure time (EXPL) were replaced with the corresponding pixels of the merged images of EXPM and EXPS. Next, the low intensity pixels of the merged images of EXPM and EXPS were replaced with pixels of the image EXPL in the final combined image. Before replacing the raw-pixel values and merging the images, the raw-pixel values of all three images were divided by their respective exposure times. The final output is a combined image HDR where both the high and low intensity regions are present as shown in figure 3.7(d).

The final combined HDR image has an effective bit depth of 24-bits which is an increase of 64-fold in the detection range compared to an 8-bits image. Now, unlike Bessel-Gaussian beam, the intensity distribution for each rings of focused Bessel-Gaussian beam do not fall off monotonically as a function of radius from the central core of the beam. Standard parameters, such as full width half maximum (FWHM) and $\frac{1}{e^2}$ beam waist, do not accurately describe the focal beam profile. Hence doing a quantitative study of the focal properties of a focused quasi Bessel-Gaussian beam becomes challenging. For this work, I am more interested in accurately

studying the focal beam profile of the central core and its immediate vicinity which is the most crucial part in optical trapping.

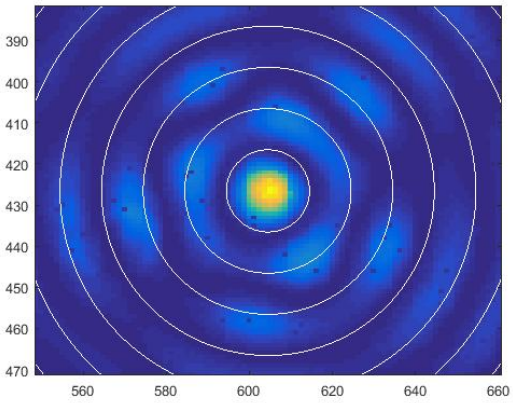

(Figure 3.8: An example of an algorithm tracing out circles over the nicely formed Bessel rings and the in-between minima.)

Now, to perform this task, for all the final HDR images taken along each axial (Z – Bessel Zone) position, the algorithm finds the central pixel location of the core and moves radially outward at regular interval tracing circles over all the concentric rings and the minima between them within a given range and taking the mean value for all of them. This step is very crucial in terms of maximizing the information captured for generating the axial focal beam profile. In an ideal scenario, I would have had the case of perfectly symmetric power distribution in the rings. But, achieving this is very challenging given the extreme precision required in the alignment of Lens-Axicon and imaging lens system and, also the effects of aberrations and manufacturing errors in lens and axicons. Hence, I have considered the possibility that if the rings in the images are not symmetrical in nature and consequently, integrating the intensity values over the non-symmetric circles for each radial value would result in a loss of information. As can be seen in figure 3.8, we have achieved a good quality Bessel beam with cylindrically symmetric rings. While the cylindrical symmetry is broken at some points, this does not appear to be a significant problem. Figure 3.8 is a zoomed image of circular ring formation as captured in CCD camera and an algorithm tracing out circles over the rings and the minima in between the rings.

3.5 Results and Analysis

3.5.1 Axial Beam Profile

In this work, I examine four different quasi Bessel-Gaussian (Bessel-like) beam profiles generated with the combination of a 30mm and a 50mm focusing lens and a 5° and a 20° axicon. The measurements were taken with a lens-axicon separation distance *d* of 8mm between the 30mm lens and both the 5° and 20° axicon and 35mm between the 50mm lens and both the 5° and 20° axicon. The lens-axicon separation distances were chosen to keep the depth of field inside the geometric focus of the lens since increasing the lens-axicon separation will decrease

the depth of field and vice versa. Consequently, the lens-axicon separation must never be larger than the focal distance of the lens. If not then, we will have a diverging beam incident on the axicon plane. Considering the geometric structure of the lens-axicon system (figure 3.1(a)), we expect to observe a couple of phenomenon. Firstly, the presence of a lens should focus the Bessel beam structure such that the width of the concentric rings and the total number of the concentric rings of the Bessel beam should decrease as we move along axial direction towards the vicinity of the geometric focus of the lens. Secondly, the Bessel core intensity should increase near the vicinity of the geometric focus of the lens. In figure 3.9, the left column shows the simulation and the right column shows the experimental result for half of the axial beam profiles generated by a 20° axicon by itself (a, b), by a $20^{\circ} - 30mm$ lens-axicon combination (c, d), by a $20^{\circ} - 50mm$ lens-axicon axicon combination (e, f), by a $5^{\circ} - 30mm$ lens-axicon combination (g, h) and by a $5^{\circ} - 50mm$ lens-axicon combination (i, j). Taking the 20° axicon as an example, a key difference that we observe is that a quasi Bessel-Gaussian beam (figure 3.9 (c, d), (e, f)) has much shorter effective propagation distance compared to Bessel-Gaussian beam (figure 3.9 (a, b)). This was expected as using focusing lens would reduce the effective propagation distance. We also observe, that the width of the concentric rings (side lobes) of the Bessel beam, i.e. each lobe narrows down and tilts, decreases as we move along axial direction towards the vicinity of the geometric focus of the lens. Next, we observe that the simulation and the experiment agree nicely only for the 20° axicon (figure 3.9 (a, b)) and also for the $5^{\circ} - 50mm$ lens-axicon combination (figure 3.9 (i, j)). In figure 3.9 (i, j), we observe a smoothly varying and elongated core intensity region. For the rest of the lens-axicon combinations (figure 3.9 (d, f, h)), we observe a sharp peak in intensity near the vicinity of the focus of the lens.

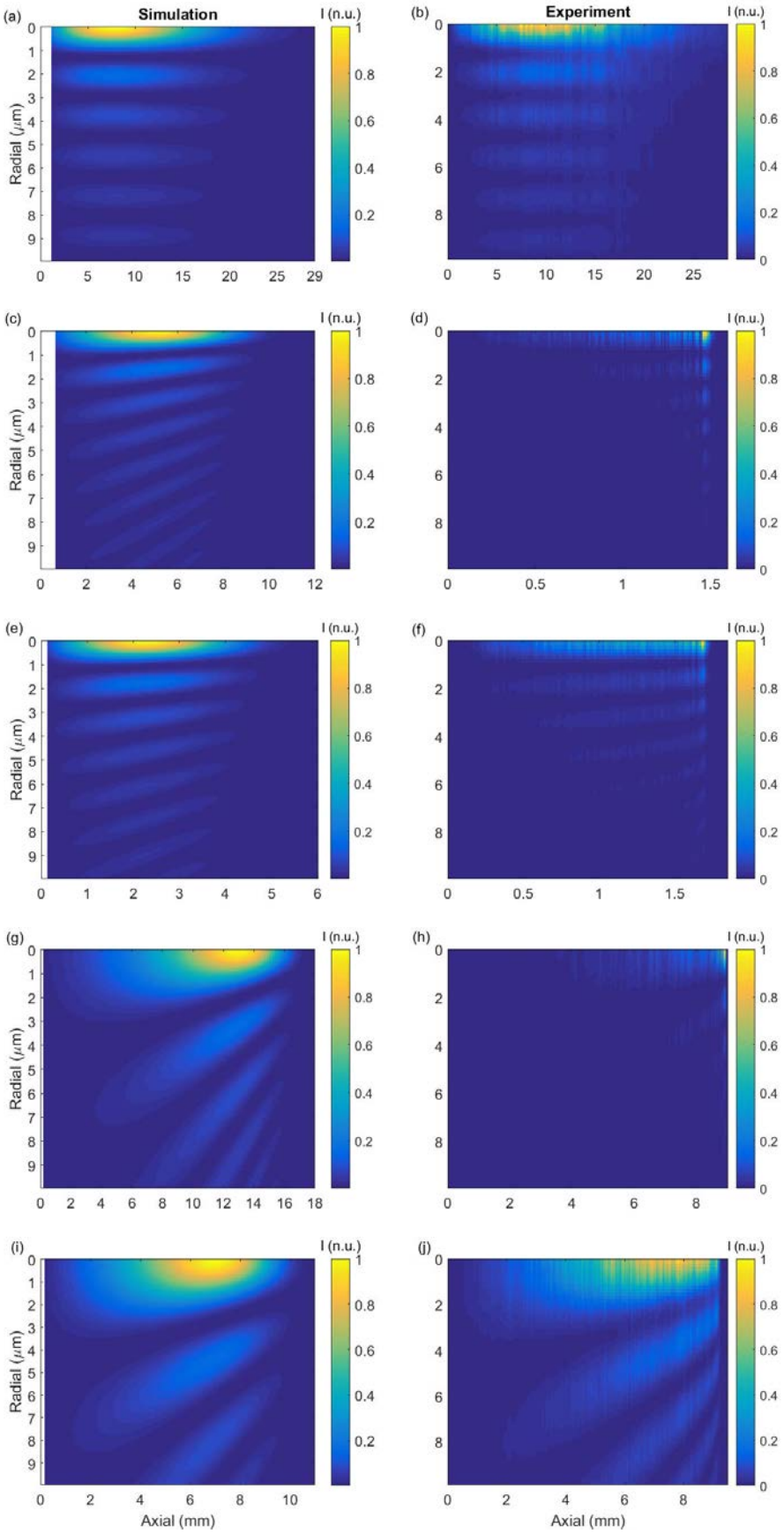

(Figure 3.9: Axial beam profile. Left column simulations and right column experiments. Images (a, b) for a 20° axicon, (c, d) for a $20^{\circ} - 30mm$ lens-axicon combination (e, f) for a $20^{\circ} - 50mm$ lens-axicon combination, (g, h) for a $5^{\circ} - 30mm$ lens-axicon combination and (i, j) for a $5^{\circ} - 50mm$ lens-axicon combination.)

3.5.2 Intensity Distribution

Figure 3.10 shows the comparison of the simulation with the experimental data for the intensity distribution of the central core (focal-line) regions generated by a 20° axicon (a), by a $20^{\circ} - 30mm$ lens-axicon combination (b), by a $20^{\circ} - 50mm$ lens-axicon combination (c), by a $5^{\circ} - 30mm$ lens-axicon combination (d) and finally by a $5^{\circ} - 50mm$ lens-axicon combination (e). Figure 3.10 (b), (c) and (d) confirms the sharp peaks in intensity in the central core region for the measurements as observed in the axial beam profiles in figure 3.9 (d), (f) and (h). Next, figure 3.10 (a) and 3.10 (e) confirms nice fitting between simulation and experiment which agrees with the axial beam profiles in figure 3.9 (a, b) and 3.9 (i, j). Comparing figure 3.10 (a) with figure 3.10 (b), (c), (d) and (e), we observe that for lens-axicon combination, the intensity peaks are shifted right towards central focal region. Also, further comparing figure 3.10 (b) with figure 3.10 (c), we observe the sharp intensity peak is slightly shifted left towards the lens-axicon system for high focusing lens as expected. Next, the sharp peak intensity regions are further investigated.

3.5.3 Bessel-Gaussian Beams Under the Presence of Spherical Aberrations

Figure 3.11 gives a closer look at the sharp peak intensity region for the lens-axicon systems. One can observe the effect of focusing Bessel beams by a lens with strong spherical aberrations in our lens-axicon systems. A closer look at the peak intensity region in figure 3.11 (a1), (a2), (b1), (b2), and (c1), (c2), we see a repeating phenomenon of increase and decrease in on-axis light intensity. For a lens with strong spherical aberration, i.e. spherical surfaces, the incoming rays will not meet in one focal point after passing through the lens. Consequently, focusing a Bessel beam with such a lens can give rise to a beating phenomenon and the repeating pattern of on-axis intensity variation is indicative of the fact.

The effect of spherical aberrations for converging lens-axicon doublets are addressed theoretically in paper (C. Parigger et al, 1997). Their system of lens-axicon doublets does not account for the lens-axicon separation that I presented in my theory. Nevertheless, their theoretical model which includes spherical aberrations predicts of the effects of lens-axicon system which corresponds to a repeating pattern of on-axis intensity variation and a short propagation distance. Their aberration-free model also predicts a smoothly varying central core intensity profile with longer propagation distances. What we observe experimentally in figure 3.11 corresponds with the theoretical predictions of the effects of spherical aberrations mentioned in the literature (C. Parigger et al, 1997).

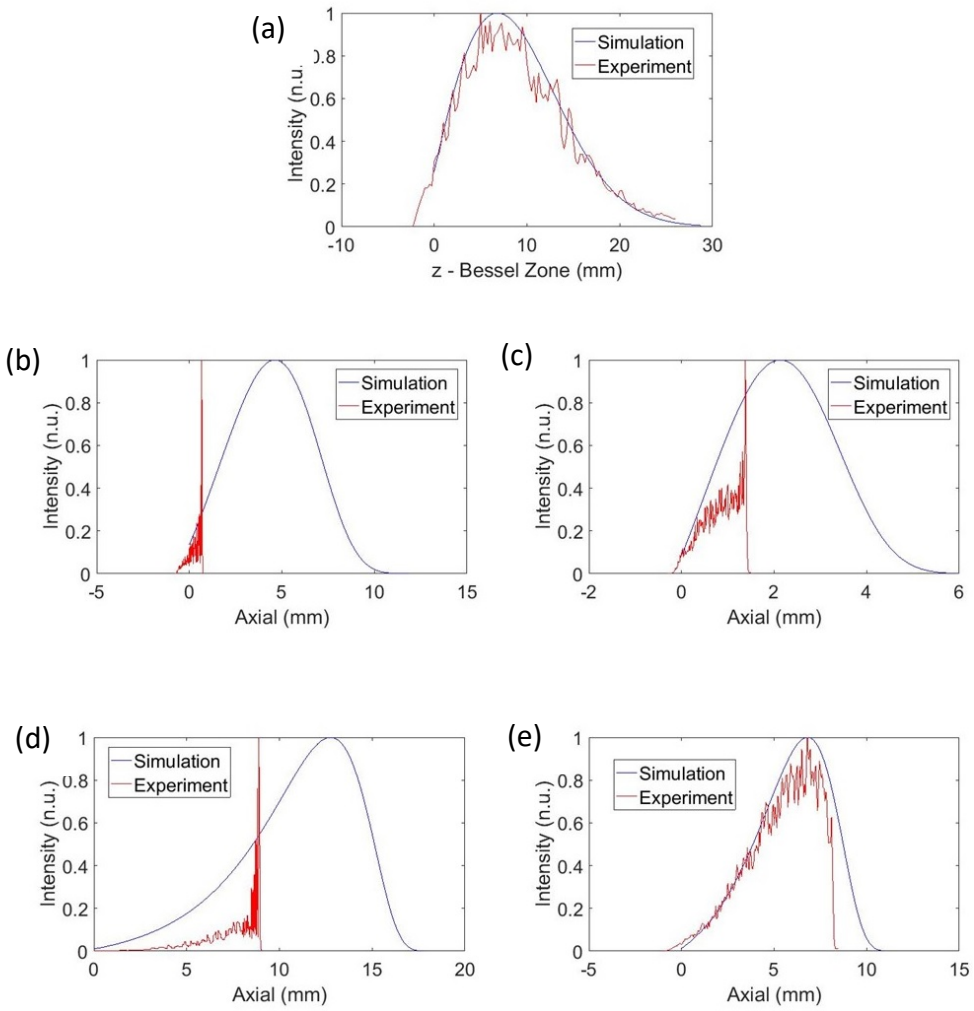

(Figure 3.10: Comparison of the simulation with the experimental data for the intensity distribution of the central core (focal-line) regions. Image (a) generated by a 20° axicon, image (b) by a $20^{\circ} - 30mm$ lens-axicon combination, image (c) by a $20^{\circ} - 50mm$ lens-axicon combination, image (d) by a $5^{\circ} - 30mm$ lens-axicon combination, and image (e) by a $5^{\circ} - 50mm$ lens-axicon combination.)

This beating phenomenon of on-axis intensity is more pronounced for both instances of using $(30\text{mm} - 20^{\circ})$ and $(30\text{mm} - 5^{\circ})$ lens-axicon combination as seen in figure (a) and (c). Here, the incoming gaussian beam is sharply focused with a lens with short focal distance and then focused again with a sharp angle axicon. The beating pattern becomes weaker as $(50\text{mm} - 20^{\circ})$ lens-axicon combination is used (figure (b)) and finally disappears as $(50\text{mm} - 5^{\circ})$ lens-axicon combination is used as seen in figure ((d)). Thus, the disappearance of the effect of such beating phenomenon of on-axis intensity for a lens with longer focal length when combined with a shallow angle axicon gives stronger indication towards the effect of spherical aberrations. We also noticed that the presence of spherical aberration for a sharp angle axicon and a lens with short focal length significantly shifts the intensity maximum towards the lens-axicon system.

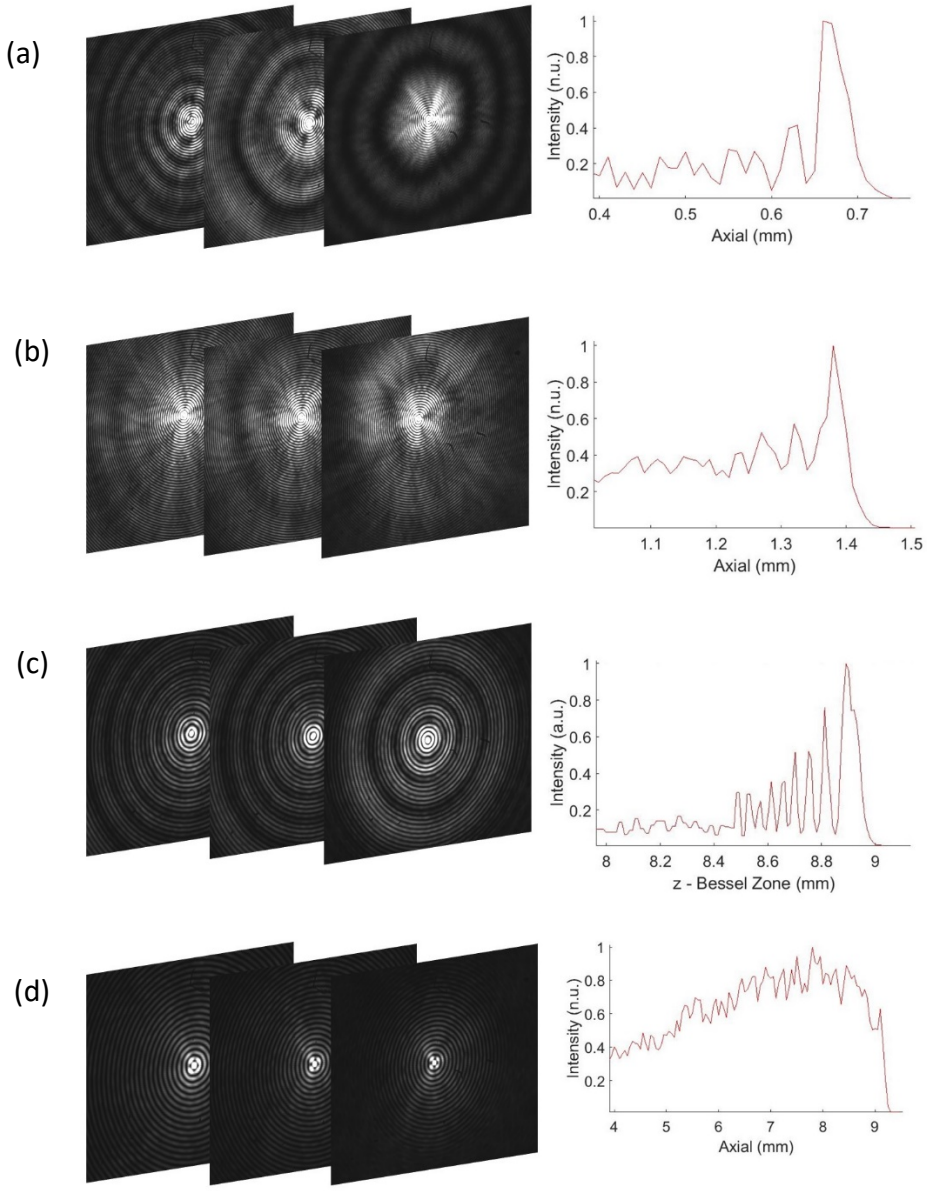

(Figure 3.11: Images corresponding to a transverse view and zoomed in axial view of the sharp peak intensity region respectively. Images (a,) for the $20^{\circ} - 30mm$, images (b) for the $20^{\circ} - 50mm$, images (c) for the $5^{\circ} - 30mm$, and images (d) for the $5^{\circ} - 50mm$.)

3.5.4 Comparison between Intensity Profiles

Next, I made a quantitative comparison of intensity profile between an axicon and lens-axicon combinations. Figure 3.12 (a) shows the MATLAB simulations of intensity profile of a 20° axicon and four different lens-axicon combinations and 3.12 (b) shows the increase in intensity for lens-axicon combination compared to the intensity of a 20° axicon from experiment.

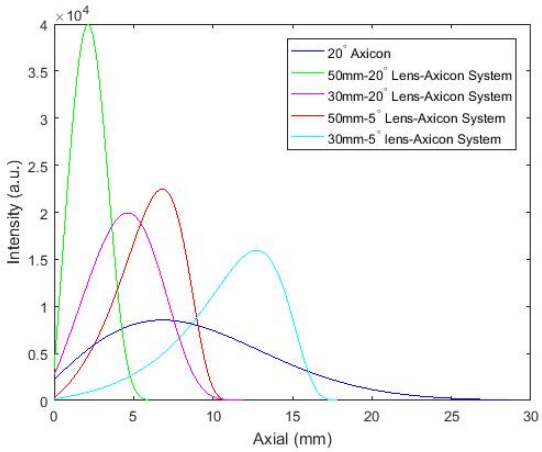

Lens-Axicon System	Intensity Increase Compared to 20° Axicon (532nm incoming Gaussian beam wavelength)
$5^\circ - 30mm$	1.87 ×
$5^\circ - 50mm$	2.63 ×
$20^\circ - 30mm$	2.33 ×
$20^\circ - 50mm$	4.67 ×

(Figure 3.12: (a) Intensity profile of a 20° axicon and four different lens-axicon combinations. (b) Table shows how much intensity in focal region of lens-axicon system increases compared to a 20° axicon.)

3.5.5 Reduction of Focal Spot Size

The final feature that I was looking for is how the focal spot sizes of lens-axicon systems changes in comparison to the spot sizes generated by sharp and shallow axicons as depicted in figure 3.13. We can see a significant reduction in the spot sizes when focusing lens are used in conjunction with a sharp 20° axicon and a shallow 5° axicon.

Axicon/Lens-Axicon System	Central Core Diameter (FWHM) for 532nm incoming Gaussian beam wavelength
5°	$5\mu m$
$5^\circ - 30mm$	$1.4\mu m$
$5^\circ - 50mm$	$2.9\mu m$
20°	$1.3\mu m$
$20^\circ - 30mm$	$0.9\mu m$
$20^\circ - 50mm$	$0.9\mu m$

(Figure 3.13: Focal spot size of axicon and lens-axicon combination)

Focal spot size (FWHM) were calculated by fitting a Bessel function with the experimental radial beam profile.

3.6 Conclusion

We see that the experimental observations of the $(50\text{mm} - 5^\circ)$ lens-axicon combination is an impressive match with the aberration-free theory. From both theory and experiment, we observe a decently long focal line of ~9.5mm and the focal region with high intensity to be ~ 4.5mm. We also observe no sign of spherical aberrations and no presence of sharp peak in intensity. Also, the focal spot size is reduced significantly compared to the focal spot size generated by the 5° axicon i.e. 1.7× smaller than the 5° axicon spot size. The other two promising combinations are the $(30\text{mm} - 5^\circ)$ lens-axicon and the $(30\text{mm} - 20^\circ)$ lens-axicon combinations. The simulation shows promising results with ~17mm and ~11mm focal lines

along with focal regions of high intensity to be ~ 7.2mm and ~ 4.8mm respectively for these two combinations. The focal spot sizes derived from the experiments for these two combinations also shows significant reductions compared to the focal spot size generated by the 5° axicon i.e. 3.6× smaller than the 5° axicon spot size and 5.5× smaller than the 5° axicon spot size respectively.

We should remind ourselves that these experiments for lens-axicon systems were performed using a 532nm diode laser and my key experiment of sensitive gravimetry deploys a 1064nm wavelength laser. Next, referring to the chapter 2, section 2.5, equation 2.42, we see that the Bessel core radius depends on radial wave vector and hence depends on wavelength of the laser. Therefore, recalling from chapter 2, section 2.7, table 2.1, the central core diameter that can be generated by the 5° axicon and 20° axicon for 1064nm wavelength is 10.4 μm and 5.2 μm respectively in my current setup. Furthermore, I have implemented optical trapping of silica particles in vertical direction using focused gaussian beam with focal beam waist of 1.99 μm (discussed in chapter 4, section 4.8). Consequently, I need to reduce the 10.4 μm or the 5.2 μm core diameter of Bessel-Gaussian beam down to a value close to 1.99 μm of focused Gaussian beam to trap the particle in the horizontal direction. To achieve this task, I need to refer to the lens-axicon system experiments performed using a 532nm wavelength diode laser and find a combination that offers either 5.2× or 2.6× reduction in central core diameter compared to a 5° axicon or 20° axicon respectively. From the lens-axicon system that I studied, I prescribe the $(30\text{mm} - 20^{\circ})$ lens-axicon combination to be the ideal candidate which offers 5.5× times reduction in central core diameter compared to a 5° axicon. But from the experiment of lens-axicon combinations, we observed that, $(30\text{mm} - 20^{\circ})$ lens-axicon combination shows effects of spherical aberrations and hence the propagation distance is reduced significantly with a strong presence of intensity peak. We can account for the spherical aberrations via numerous means such as using aspheric lens, large lenses, etc. and deploy this combination in my setup for generating counter-propagating Bessel-Gaussian beams.

In this chapter, I have characterized the beam profile of a lens-axicon system. Both theory and observation show that the effective propagation distance, spot size and on-axis central core intensity can be significantly tuned using a sharp and a shallow axicon, a focusing lens and changing the distance between the lens and the axicon. It is shown that using lens with strong spherical aberration, the propagation distance is reduced significantly with a strong presence of intensity peak. The spherical aberrations can be accounted for via numerous means such as using aspheric lens, large lenses, etc. Using a suitable choice of apex angle axicon, aberration free optical lens and a suitable lens-axicon separation distance, we can tune the

quasi Bessel-Gaussian beam to suit my experimental needs. This study is very encouraging for the application of quasi Bessel-Gaussian beams for optical trapping applications.

Chapter 4

Initial Implementation of Optical Trapping

In the previous chapter, I investigated the properties and highlighted the promising potential of trapping with Bessel-like beams. In this chapter, I present the design and development of my optical trapping setup. The initial implementation of my custom designed trapping setup will be conducted in air to implement the trapping of levitated nanoparticles along horizontal direction using counter-propagating Bessel-like beams experimentally and to study the trapping forces due to these special beams. Future objective is to implement a similar trapping scheme in vacuum to perform sensitive gravimetry by using the information we learn in this experiment.

In this chapter, specific attention is given to the key active participants in the constructions of this trapping system which includes a specially designed trapping chamber, an imaging system to monitor the comprehensive motion of the particle within the trapping chamber, and a motion detection system to measure the position of the trapped particle. I discuss my unique custom designed system which facilitates two distinct optical trapping schemes which are orthogonally aligned. The initial trapping of nanoparticles is performed vertically using highly focused Gaussian beam and subsequent trapping is performed by keeping the particle trapped using two horizontally counter propagating special Bessel-Gaussian beam as the vertical Gaussian beam is gradually switched off. The key motivation behind this two-way trapping design is that along the given horizontal direction of the two-counter propagating special beam, we will have a net zero scattering force and a slowly varying dipole force making the particle extremely sensitive to any applied external force. The reason for choosing the horizontal direction for trapping with the two-counter propagating special beam is due to the ease of control in alignment. In this initial implementation of trapping in air, I will be studying the sensitivity by minimizing the gradient force along the propagation direction using Bessel-Gaussian beams. But to perform sensitive gravity measurements, trapping of nanoparticles using two counter-propagating Bessel-Gaussian beam needs to be done along the vertical directions.

4.1 Experimental Setup of Optical Trapping

Figure 4.1 shows the schematics of the optical trapping setup.

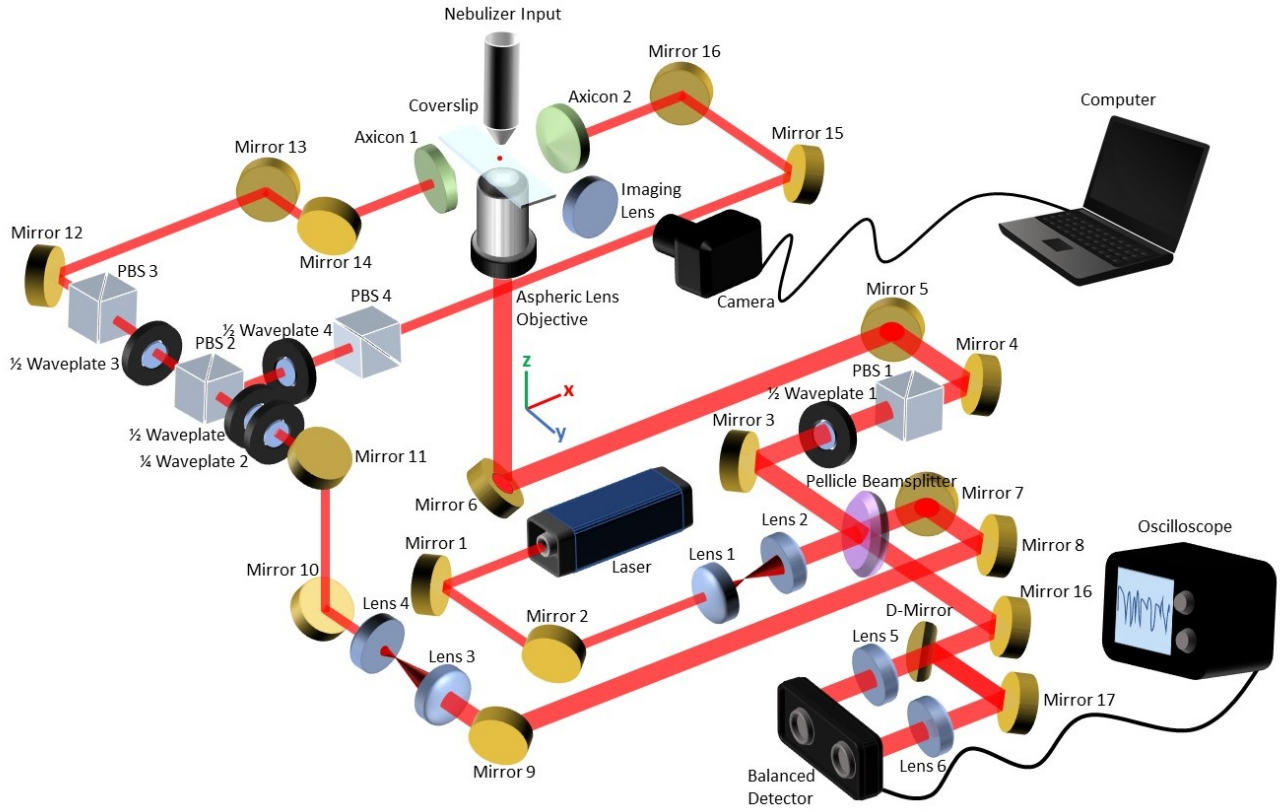

(Figure4.1: Schematic representation of the optical trapping setup. See details in the text.)

The setup consists of two optical trapping segments using the same continuous wave 1064nm Neodynium: YAG laser (Ventus 1064, Laser Quantum). In the first section, the 1064nm trapping laser beam is expanded and collimated by a telescope formed by lens1 and lens2 and then the collimated beam is incident on a pellicle beamsplitter angled at 45° to reflect 190mW and to transmit 1.45W of laser beam. The reflected 190mW beam is then incident on a half waveplate and then a polarizing beam splitter (PBS – BP133, Thorlabs). By rotating the half waveplate, the laser power is controlled while maintaining horizontal polarization through the PBS. The beam is then aligned and incident on the back entrance of the aspheric lens. The beam is expanded to slightly overfill the back aperture of the aspheric lens and the beam is then focused by the aspheric lens to form a near diffraction limited stable trap 1.76 mm away from the surface of the lens. The beam needs to be symmetric about the vertical focal direction to make the trap stable. This is achieved through careful adjustment of mirror4 and 5 that lead to the aspheric lens so that the center of the beam passes precisely through the middle of the aspheric lens. The backscattered light from the trapped particle is then collected with the same aspheric lens and following the same path to the pellicle beam splitter and transmitted through to the balanced detector. An imaging source is employed to record the trapping process at 4 ×

magnification using a 30mm lens and a CCD camera. All the mirrors (PF10-03-P01) used throughout the setup are highly reflective at 1064nm and hence reflects 100% of the laser beam.

The second section of the setup treats the remaining 1.45W of laser beam, transmitted though the pellicle beam splitter. The transmitted beam through the pellicle beam splitter is then directed towards another telescope formed by lens3 and lens4 using mirrors where it is reduced and collimated again. The introduction of the lens pair 3 and 4 at this stage is crucial since with them the incoming Gaussian beam diameter can be varied to any arbitrary value to modulate the Bessel-Gaussian beam profile i.e. increase or decrease the Bessel zone and increase or decrease the number of Bessel rings. The reduced and collimated beam is then incident upon half waveplate and then the quarter waveplate and then onto PBS2. By controlling the waveplates, the beam can be split exactly in half using PBS2 and eventually directed towards axicon 1 and 2. If the beam is not split into exact half, then one half of the beam will have more intensity which will result in one of the Bessel-Gaussian beam having different spatial and tangential beam profiles resulting in an unstable trap. The transmitted half of the beam through PBS2 is then incident on waveplate3 and then onto PBS3. Using mirrors, the beam through PBS3 is then reflected horizontally towards axicon1. By adjusting mirror13 and 14, the beam leading to axicon1 can be precisely aligned. By rotating half waveplate3, the beam power is precisely controlled. Now, the remaining reflected half of the beam off PBS2 is then incident on waveplate4 and then onto PBS4. PBS4 is positioned perpendicularly in relation to PBS3 to make the transmitted beam through PBS4 cross-polarized in relation to the transmitted beam through PBS3. This is done because having same polarization will result in interference effect with the counter-propagated Bessel-Gaussian beam resulting in a drastic reduction of the trap length for this experimental purpose. The beam is then reflected using mirrors in horizontal direction towards axicon2. Again, by adjusting mirror15 and 16, the beam leading to axicon2 can be precisely aligned and by rotating half waveplate4, the beam power can be precisely controlled.

Now the Bessel-Gaussian beam generating off the tip of axicon1 and 2 must be aligned with extreme precision to trap the particle in the horizontal direction. Once the central core of the counter-propagating Bessel-Gaussian is perfectly aligned along the horizontal axis of the trapped particle, by rotating the half waveplate1, the vertical trapping beam can be completely switched off with the aim of keeping the particle trapped with the two counter-propagating Bessel-Gaussian beams. A quick look at the specifications of the pellicle beam splitter which splits the laser beam into two segments is presented next.

4.2 Beam Splitter

In this work, a 1" Pellicle beamsplitter is used (BP133, Thorlabs). The beam splitter reflects 15% of the power to the vertical trapping at the focus and to the motion detection and transmits 85% to the counter-propagating beam (power going to the axicons) at 1064nm wavelength. The setup was designed to maximize the power that is required for the counter-propagating beam and since only 15% of the total power was sufficient for vertical trapping at the focus, a low reflective beam splitter was deployed. A low reflection pellicle beamsplitter is also advantageous for our detection scheme, since most of the back reflected detection signal is transmitted towards the balanced detector. In the next section, I present my choice of focusing lens for initial vertical trapping of nanoparticles.

4.3 Aspheric lens for vertical trapping

The lens used for trapping is molded glass aspheric lens – C330TMD-B, Thorlabs. It has a high numerical aperture (NA) of 0.68, an effective focal length of 3.1 mm and a working distance between the lens and focal point of 1.76 mm. It is anti-reflection coated for a diffraction-limited performance over a broad spectral range, between 650 – 1050 nm, to ensure most of the radiation passes through. The same lens is used to focus the optical tweezer beam at 1064 nm range and to collect the back-reflected light at 1064 nm from the trapped particle.

When a nebulized particle drifts near the focus of the beam, the gradient force will either pull or push the particle towards the high intensity region depending on the drifting particle being above or below the focal plane. This restoring force is required for trapping. Whereas, the scattering force pushes the particle towards the beam propagation direction and hence does not have any restoring force. Consequently, optical trapping is possible when the gradient force overcomes the scattering force. Therefore, high numerical aperture optics are required to produce strong enough gradient force which can trap particle in air (B. Redding et al, 2015, R. Omori et al, 1997). The choice of the trapping objective is directly related to the trapping efficiency.

A high NA microscope objective would have been an ideal choice for trapping. But I chose aspheric lens for couple of reasons. Firstly, I require a smaller diameter trapping objective. This is because the Bessel zone for my counter propagating Bessel-Gaussian beam is ~ 9.5 mm which is smaller than the typical microscope objective diameter (~20mm). Secondly, the working distance of high NA microscope objective is ~ 0.2 mm and I require much longer working distance for my trapping objective so that it does not significantly clip the Bessel beam. We already saw in chapter 2 section 2.6.4 that Bessel beams have self-healing properties. But in

this case, the Bessel zone is smaller than the objective lens diameter. This means that the Bessel-Gaussian beam will not be able to self-reconstruct itself. Besides having high NA and longer working distance lens, an Aspheric lens also made an excellent choice for the following reason. The surface of an aspheric lens is designed in such a way that it eliminates spherical aberrations, disturbance at the focus of the lens, resulting in a diffraction limited spot size. Spherical aberration is the deviation of the focal point of the spherical lens due to thickness of the lens. Eliminating spherical aberration is crucial to optical trapping since it will allow us to produce a near perfect stable trapping potential as discussed in theory section. The next section briefly presents the optical elements used in the experiment to generate counter-propagating Bessel-Gaussian beams and to precisely control the alignments of counter-propagating beams.

4.4 Axicon and 5-axis Mounts

Figure 4.2 shows an image of an axicon mounted on a 5-axis kinematic mount.

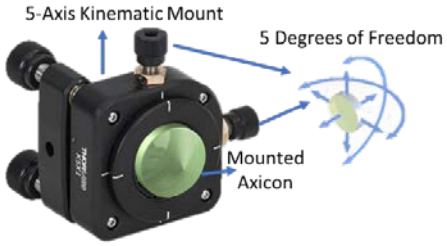

(Figure 4.2: Image of an Axicon mounted on a 5-axis kinematic mount with 5 degrees of freedom for precision alignment)

Two very sharp angle axicon 20° (UV fused Silica – AX2520-C, Thorlabs) are used in the setup with the aim of generating counter propagating Bessel-Gaussian beams. Along the counter propagating direction, the scattering force can be cancelled out (M. Guillon et al, 2005, T. Li, 2013, B. Redding et al, 2015). Achieving this will be challenging and will require precision in alignment. To meet such needs, the axicons are mounted on 5-axis (K5X1, Thorlabs) kinematic mounts which offers 5 degrees of freedom along 5 axes i.e. X, Y, Z direction, pitch and paw. It features:

- Pitch/Yaw: ±4° at 8 mrad/rev.
- X and Y translation: ±0.04" (±1.0mm) at 250.0µm/rev.
- Z translation: ±0.13" (±3.2 mm). Operation is performed by turning all 3 tip/tilt adjusters.

4.5 Trapping Chamber

I custom designed the trapping chamber in the form of a cuboid bounded by six quadrilateral faces. It was drawn using 3D CAD Design Software (Solidworks) and attached in the appendix.

The depth/width of the cuboid is 19mm with the wall being 2mm thick. Both front and back faces have 20mm diameter hole symmetrically positioned. Axicons facing each other separated by 15mm in length is positioned along the centers of the holes. Coverslips of 22mm × 22mm is attached to the inner side of the walls to protect the axicons and to seal the chamber. A compromise of 4mm effective counter-propagating Bessel-Gaussian zone is achieved given the dimension of the diameter of the Aspheric lens and the Bessel zone produced by each axicons. The left face of the cuboid is cut open and sealed with a 19 × 30mm coverslip for ccd imaging. The right side of the chamber has a slit of 4mm in height and 14mm in width through which a coverslip can enter and sit on top of the aspheric lens to protect the lens from nebulized particles. A circular hole of 13mm is made at the bottom face of the chamber to house the mounted aspheric lens system of 11mm in diameter. A circular hole of 11mm is made at the top face of the chamber to house a nebulizer.

The figure 4.4 below contains (a) schematics of the cuboid chamber and (b)real images.

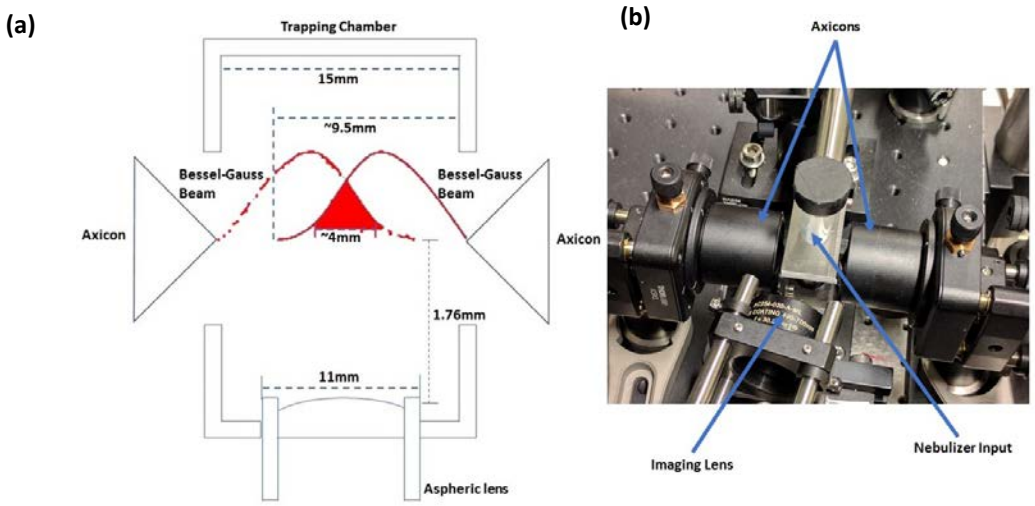

(Figure 4.4: (a) Schematic representation of the trapping chamber with the left side facing us and the front and back side facing right and left consecutively where the two axicons are stationed. Both axicons produce a Bessel zone of ~9.5mm. Given the transverse dimension of the Aspheric lens of 11mm, a compromised overlapping Bessel zone of ~4mm is achieved for counter propagating trapping scheme. The Aspheric lens has a 1.76mm of working distance. (b) A close-up top view of the chamber with Axicons, CCD camera and nebulizer.)

The main nanoparticles that were trapped throughout the experiments are Silica particles of an average size of 150nm and 300nm. Particle solutions were made by diluting different concentration of Silica particles until the best solution combination is found. The solution was always sonicated for at least 30 minutes prior to trapping to disperse individual Silica crystals. The diluted Silica solutions are sprayed into the chamber and the particles then slowly drift into the focus of the laser beam. The focused beam then can apply forces on the

particles and trap them at the focus. Particles that are below the focus of the beam are pushed upwards towards the focus due to scattering force. Whereas, particles above the focus of the beam pushed away from the focus towards the top surface of the chamber and drifting away due to Brownian motion. Hence dipole force must supersede scattering force and pull the particle towards the focus. Caution must be applied while vertically positioning the coverslip. The coverslip must be positioned below the focus of the beam close to the surface of the lens. Figure 4.5 (a) shows the propagation of scattering force and (b) shows the positioning of the coverslip.

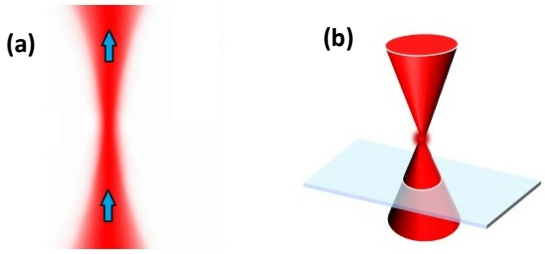

(Figure 4.5: (a) Diagram showing the direction of propagation of the scattering force and (b) Diagram showing the positioning of the coverslip)

The following two sections considers the position detection scheme i.e. a low-resolution CCD camera to detect the particle as it gets trapped inside the trapping chamber and high bandwidth balanced detector for high frequency position measurements.

4.6 Position Detection – CCD Camera

A video based imaging system consisting of a CCD camera (LU165M, Lumenera) is deployed in this setup. When a particle is trapped at the center of the focus, it is possible to reconstruct the high intensity and rapidly oscillating diffraction limited image of the particle on the CCD using Fourier optics, i.e. the imaging lens, using the scattered photons from the particle (figure). This allows us to observe a particle when it is trapped at the focus. It would typically take seconds and even sometimes up to minutes for a particle, drifting in air due to Brownian motion, to enter the trap depending upon the dilution of the sample. The sample solution needs to be more diluted if you need to keep the particle trapped and characterize its properties for longer time. A high concentration solution will tend to prevent trapping of particles for longer period due to other particles hitting the trapped particles. However, the waiting period for achieving trapping increases as the solution becomes more diluted. A snapshot of a trapped Silica particle is seen in figure 4.6.

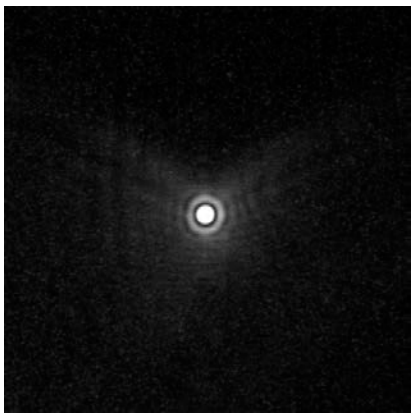

(Figure 4.6: Image of a trapped Silica particle observed on the CCD camera. The trapping laser is incident on the Silica particle and the particle is trapped at the focus. The bright spot is an example of quickly oscillating diffraction limited spot of the back-reflected light of the Silica.)

Deploying numerous centroid fitting algorithm, the position of the trapped particle can be determined within sub pixel accuracy (J. C. Crocker et al, 1996, M. K. Cheezam et al, 2001, and R. E. Thompson et al, 2002). In this work, real time video tracking is implemented (C. Gosse et al, 2002, and M. Keller et al, 2001). But it is limited by the frame rate (25Hz) of the CCD camera. Although such low resolution of the CCD camera is poor for position detection but enough for nebulizing and imaging of the particle. To obtain high frequency position measurements, a high bandwidth balanced detector is deployed.

4.7 Position detection – Balanced Detector

A balanced detector is a device that performs precision measurements of small differences in the intensity of the beams. It consists of two photodetectors that can measure the intensity of two incident laser beams and can produce a voltage which is proportional to the differences in their intensities up to some given cut-off voltage. Following figure 4.7 depicts a schematic of a balanced detector measuring the position of trapped particle.

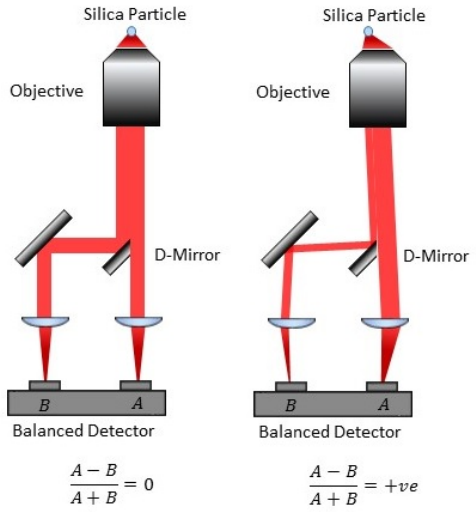

(Figure 4.7: Schematic showing how the movement of the Silica particle affects the signal of the balanced detector. When the particle is displaced from the beam axis, the beam power preferentially favors one of the detectors and therefore the difference signal gives a non-zero reading.)

When a particle is trapped at the center of the trap, the back scattered and recollimated beam from the particle is symmetrically distributed around the center of the back aperture of the objective. In my setup, a D-mirror (BBD1 – E03, Thorlabs) positioned on a 1D translation stage, is used to split half the back reflected beam in exact proportion such that the difference in signal becomes zero.

As the oscillating trapped particle moves to one side of the trap, the back reflected light is no longer symmetric around the center of the back aperture of the objective. Consequently, the D-mirror splits the back reflected beam unevenly and one half of the beam ends up having more intensity relative to the other. Such uneven splitting of the beam results in an amplified signal by the balanced detector which is linear to the trap position. As it oscillates back to the other side of the trap, a negative voltage is recorded on the other photodetector. According to general consensus found in the literatures (F. Gittes et al, 1998, K. C. Neuman et al, 2004, M. J. Lang et al, 2002), the position detector should be placed in the back focal plane (BFC) or at an optical plane conjugate to the BFC, rather than at an imaging plane conjugate to the trapped particle, in order to achieve precise, high-bandwidth position detection of the trapped particle. This BFC detection scheme relies on the interference between the scattered light from the trapped particle and the un-scattered light, instead of relying solely on the scattered light from the particle, and consequently this interference light is monitored with the position detector described as above. The benefits of imaging the BFC is that the position detection signal becomes insensitive to the absolute position of the particle in the particle plane and rather becomes sensitive to the relative displacement of the particle from the laser beam axis (A. Rohrbach et al, 2002, F. Gittes et al, 1998, K. C. Neuman et al, 2004, M. J. Lang et al, 2002). In my setup, the D-mirror is placed at an optical plane conjugate to the BFC and the interference signal from the scattered light of the particle and the reflected light from the coverslip is measured at the balanced detector. An example of a voltage signal of an optically trapped Silica in air is shown in figure 4.8.

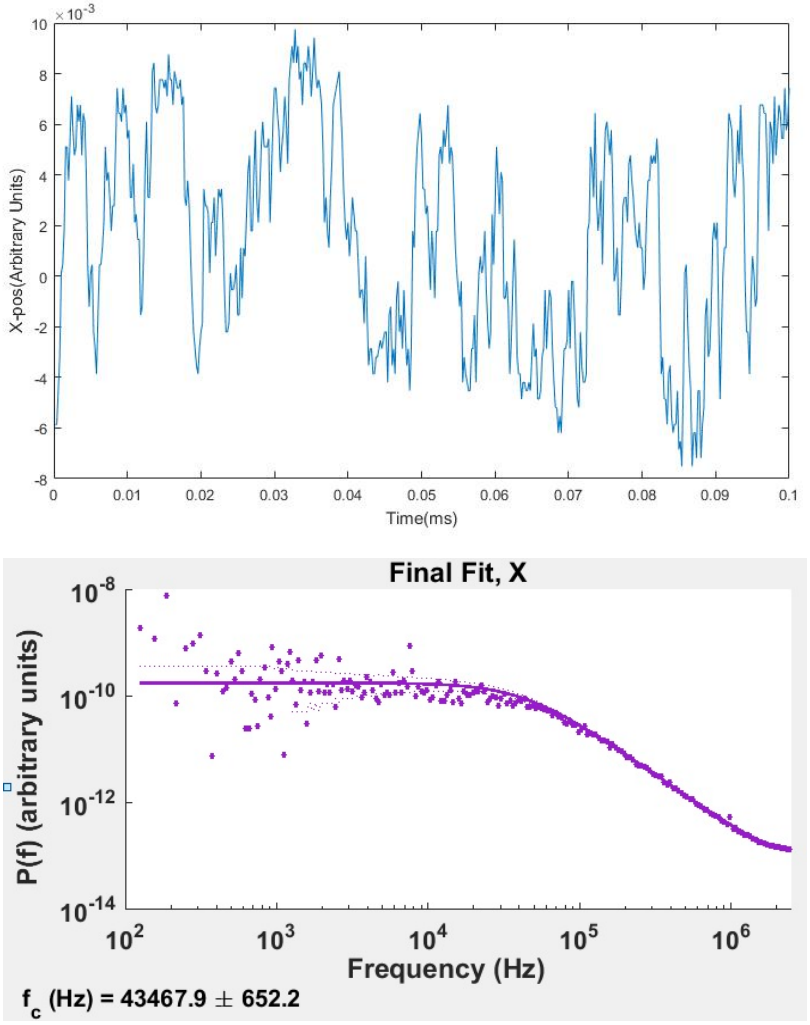

(Figure 4.8: Position measurements of an optically trapped Silica particle and power spectrum density of a trapped Silica particle. The MATLAB software tweezercalib 2.0 was used to generate the plot and fit the Lorentzian curve (solid line) to the data)

I present the trapping frequency obtained for the optically levitated and trapped Silica particle. In this optical trap, the absolute trapping stiffness value is not usually calculated and only the corner frequency is investigated. A MATLAB software package named tweezercalib 2.0 (P. M. Hansen et al, 2006) designed for precise calibration of optical tweezers is deployed to evaluate the trapping frequency. Figure 4.8 shows an example of a power spectrum density of a trapped Silica particle analyzed by the tweezercalib 2.0. The software fits a Lorentzian profile to the data to produce the corner frequency value of the trapped Silica particle. Using equation 2.27, the trapping stiffness value can be evaluated. For this Silica particle, the corner frequency was 43500 ± 700Hz.

4.8 Trapping Powers

In my current setup, I have allocated 190mW of laser power for the vertical trapping of Silica particles and trapping occurs between 63mW-127mW of laser power with 1.99μm beam waist

diameter for my Aspheric lens. The rest of the 1450mW of power is divided amongst the two axicons with 725mW of power for each axicon. As discussed in chapter 2, the beam of 3mm in diameter is incident on each of the 20° axicon in the setup and will produce a Bessel beam core of 5.2μm in diameter and 288 concentric rings. Also recalling from chapter 2, the power is equally distributed amongst central core and each concentric ring. Therefore, each Bessel beam will have 2.5mW of power in its core. Deploying suitable lens-axicon combination as discussed in chapter 3, I can significantly reduce the 5.2μm core and increase the central core intensity. But to match the 63mW-127mW of trapping power, I will also need a higher power laser source in combination with a lens-axicon system.

Chapter 5

Conclusion and Future Work

In the next stage of this project, I plan to realize my proposed solution of using a suitable lens-axicon combination along with a high-power laser source for trapping a Silica particle with counter-propagating Bessel-Gaussian beam. The duration of my Master of Research project was for only 8 months. Given such a short timeframe, it was not possible to apply the proposed solutions and to test the trapping of nanoparticles using counter-propagating Bessel-Gaussian beams and perform the sensitivity tests.

5.1 Conclusion

My long-term objective is to implement a sensitive gravimetry system based on levitated nanoparticles cooled to the quantum regime. I propose a design that utilizes special diffraction-free counter-propagation beams for the optical trapping of nanoparticles and improves the sensitivity by releasing the gradient force along the propagation direction of the beams while keeping the particle trapped in the transverse plane. Bessel-Gaussian beams are an ideal choice for achieving this.

I started my project by studying the nice diffraction-free propagation and self-healing properties of the Bessel beams. Next, I studied the possibilities of trapping with Bessel beams. The inherent structure of the Bessel beams consists of a central core and many concentric rings and the total power of the beam is equally distributed amongst the core and the outer rings. Optical trapping of nanoparticles requires a relatively tight focal spot size since a small focal point will have stronger gradient force which will keep the particle trapped at the focus.

Achieving this with Bessel beams as well as maintaining a longer diffraction-free propagation distance is a significant challenge. Additionally, longer propagation distances mean we would have large number of concentric rings, which in turn would decrease the central core intensity. To address the challenge, I studied the spatial characterization of the Bessel-Gaussian beam and observed that focusing Bessel-Gaussian beams too much with high angles results in aberrations. Consequently, I offered a simple and compact solution to reduce the central core spot size of the Bessel-Gaussian beams as well as maintaining a long effective propagation distance with increased core intensity and offered solutions for aberrations.

Next, with all the information at hand, I designed and performed an initial implementation of the optical trap and successfully trapped Silica particles using a highly focused Gaussian beam along the vertical direction. Now, the next step would be to keep the nanoparticles trapped using counter-propagating Bessel-Gaussian beams along horizontal direction. To realize this, I need to tailor the central core spot size and match the power of the central core of the counter-propagating Bessel-Gaussian beam to that of the focused Gaussian beam. Therefore, I propose the use of a suitable lens-axicon combination along with higher power laser source with which I can achieve the trapping of nanoparticles using counter-propagating Bessel-Gaussian beams.

During the next phase, I plan to implement the proposed solution of using a lens-axicon system and a higher power laser source. With the solution being implemented, the counter propagating Bessel-Gaussian beams will be turned on along transverse direction and the focused Gaussian beam intensity will be gradually lowered down to zero. The dipole force along the propagation axis of the two counter-propagating Bessel beams will be insignificant, hence giving the trapped particle freedom to move along that preferred axis without any hinder. The particle is optically levitated and trapped and decoupled from the external environment. It will be extremely exciting to observe the movement of the particle as we tune the Bessel beam intensity from both end along the Bessel beam propagation axis to push the particle towards the trapping center. Once we obtain the experimental results, we expect to be in a position of submitting a manuscript to a scientific journal. The experimental result of this project will hopefully pave the pathway to levitate massive dielectric particles in vacuum for sensitive Gravimetry which I plan to undertake in the coming three years.

Chapter 6

Bibliography

1) A. Geraci, S. B. Papp, and J. Kitching, 2010, "*Short-range force detection using optically cooled levitated microspheres*.", arXiv:1006.0261

2) Arvanitaki and A. A. Geraci, 2013, "*Detecting high-frequency gravitational waves with optically levitated sensors*.", Phys. Rev. Lett., vol. 110, p. 071105

3) Ashkin and J. M. Dziedzic, 1971, "*Optical levitation by radiation pressure.*", Applied Physics Letters, Vol. 19, pp. 283 – 285

4) Ashkin, J. M. Dziedzic, 1975, "*Optical levitation of liquid drops by radiation pressure.*", Science, Vol. 187, Issue 4181, pp. 1073-1075

5) Ashkin J. M. Dziedzic, 1976, "*Optical levitation in high-vacuum*.", Appl. Phys. Lett. Vol. 28, pp. 333–335

6) Ashkin J. M. Dziedzic, 1977a, "*Feedback stabilization of optically levitated particles*.", Appl. Phys. Lett. Vol. 30, pp. 202–204

7) Ashkin J. M. Dziedzic, 1977b, "*Observation of resonances in radiation pressure on dielectric spheres.*", Phys. Rev. Lett. Vol. 38, pp. 1351–1354

8) Ashkin J. M. Dziedzic, 1985, "*Observation of radiation-pressure trapping of particles by alternating light-beams.*" Phys. Rev. Lett. Vol. 54, pp. 1245–1248

9) Ashkin J. M. Dziedzic, J. E. Bjorkholm, S. Chu, 1986, "*Observation of a single beam gradient force optical trap for dielectric particles.*", Opt. Lett. Vol. 11, pp. 288–290

10) Ashkin, 1970, "*Acceleration and trapping of particles by radiation pressure*.", Phys. Rev. Lett. Vol. 24, pp. 156 – 159

11) Ashkin, 1970, "*Atomic-beam detection by resonance-radiation pressure*.", Phys. Rev. Lett. Vol. 25, pp. 1321 – 1324

12) Ashkin, 1992, "*Forces of a single-beam gradient laser trap on a dielectric sphere in the ray optics regime*.", AT&T Bell Laboratories, Holmdel, New Jersey 07733

13) Ashkin, J.M. Dziedzic, 1987a, "*Optical trapping and manipulation of viruses and bacteria.*", Science Vol. 235, pp. 1517

14) Ashkin, J.M. Dziedzic, T. Yamane, 1987b, "*Optical trapping and manipulation of single cells using infrared laser beams.*", Nature Vol. 330, pp. 769

15) Aspect, E. Arimondo, R. Kaiser, N. Vansteenkiste, and C. Cohen-Tannoudji, 1988, "*Laser cooling below the one-photon recoil energy by velocity-selective coherent population trapping*.", Phys. Rev. Lett. Vol. 61, pp. 826 – 829

16) E. Siegman, 1986, "*Lasers*", university science books, Mill Valey, Calif, pp. 640

17) Jesacher, S. Furhapter, S. Bernet, M. Ritsch-Marte, 2004, "*Diffractive optical tweezers in the Fresnel regime.*", Opt. Express Vol. 12, pp. 2243 – 2250

18) Nussbaum and R. A. Phillips, 1976, "*Contemporary Optics for Scientists and Engineers.*", Prentice-Hall, Englewood Cliffs, NJ, pp. 243.

19) Stockham, J. G. Smith, 2006, "*Optical design for generating Bessel beams for micromanipulation.*", Proc. SPIE Vol. 6326

20) Adam M. Summers, Xiaoming Yu, Xinya Wang, Maxime Raoul, Josh Nelson, Daniel Todd, Stefan Zigo, Shuting Lei, and Carlos A. Trallero-Herrero, 2017, "*Spatial characterization of Bessel-like beams for strong-field physics.*", Optics Express Vol. 25, pp. 1646-1655

21) Alexander Rohrbach and Ernst H. K. Stelzer, 2002, "*Three-dimensional position detection of optically trapped dielectric particle.s*", Journal of Applied Physics Vol. 91, pp. 5474

22) Brandon redding and Yong-le pan, 2015, "*Optical trap for both transparent and absorbing particles in air using a single shaped laser beam.*", Optics Letters Vol. 40, pp. 2798 – 2801

23) Gosse and V. Croquette, 2002, "*Magnetic tweezers: micromanipulation and force measurement at the molecular level.*", Biophys. J. vol. 82, pp. 3314 – 3329

24) Parigger, Y. Tang, D. H. Plemmons and J. W. L. Lewis, 1997, "*Spherical Aberration Effects in Lens-Axicon Doublets: Theoretical Study.*", Applied Optics, Vol. 36, pp. 8214 – 8221

25) E. Chang, C.A. Regal, S.B. Papp, D.J. Wilson, J. Ye, O. Painter, H.J. Kimble, P. Zoller, 2010, "*Cavity opto-mechanics using optically levitated nanosphere.",* PNAS Vol. 107, pp. 1005–1010

26) D. McGloin, K. Dholakia, 2005, "*Bessel beams: diffraction in a new light.",* Contemporary Physics Vol. 46, pp. 15-28

27) D. Sheng, S. Li, N. Dural, M. V. Romalis, 2012, "*Sub-femtotesla scalar atomic magnetometer using multipass cells.*", arXiv:1208.1099

28) Diedrich, J. C. Bergquist, W. M. Itano, and D. J. Wineland, 1989, "*Laser cooling to the zero-point energy of motion.*", Phys. Rev. Lett. Vol. 62, pp. 403 – 406

29) Gittes and C. F. Schmidt, 1998, "*Interference model for back-focal-plane displacement detection in optical tweezers*.", Opt. Lett. Vol. 23, pp. 7 – 9

30) F. Gori, G. Guattari, C. Padovani, 1987, "*Bessel-Gauss Beams.*", Optics Communications Vol. 64, pp. 485 – 574

31) Freescale Accelerometer Product Chart (http://www.nxp.com)

32) Grynberg, A. Aspect, and C. Fabre, 2010, "*An Introduction to Quantum Optics: From the Semi-Classical Approach to Quantized Light*.", Cambridge University Press.

33) G. Roosen and C. Imbert, 1976, "*Optical levitation by means of 2 horizontal laser beams-theoretical and experimental study*.", Physics. Lett. Vol. 59, pp. 6-8

34) G. Roosen, 1979, "*Optical levitation of spheres.",* Can. J. Phys. Vol. 57, pp. 1260 – 1279

35) Fernandez-Corbaton, X. Zambrana-Puyalto, N. Tischler, A. Minovich, X. Vidal, M. L. Juan, G. Molina-Terriza, 2013, "*Electromagnetic duality symmetry and helicity conservation for the macroscopic Maxwell's equations*.", arXiv:1206.0868

36) A. Stratton, 1941, "*Electromagnetic theory*", McGraw-Hill, New York, pp. 175-176, 205-207

37) Arlt, K. Dholakia, 2000, "*Generation of high-order Bessel beams by use of an axicon*", Optics Communication Vol. 177, pp. 297 – 301

38) J. Arlt, V Garces-Chavez, W Sibbett, K Dholakia, 2001, "*Optical micromanipulation using a Bessel light beam.*", Optics Communication Vol. 197, pp. 239 – 245

39) J. C. Crocker and D. G. Grier, 1996, "*Methods of digital video microscopy for colloidal studies.*", Journal of Colloid and Interface Science Vol. 179, pp. 298 – 310

40) J. Chaste, A. Eichler, J. Moser, G. Ceballos,R. Rurali & A. Bachtold, 2012, "*A nanomechanical mass sensor with yoctogram resolution*.", Nature Nanotechnology Vol. 7, pp. 301–304

41) J. Chen, J. Ng, Z. Lin, C. T. Chan, 2011, "*optical pulling force.",* Nature Photonics Vol. 5, pp. 531

42) J. Dalibard and C. Cohen-Tannoudji, 1989, "*Laser cooling below the doppler limit by polarization gradients: simple theoretical models*.", J. Opt. Soc. Am. B Vol. 6, pp. 2023 – 2045

43) J. Durnin, 1987, "*Exact solutions for nondiffracting beams. I. The scalar theory.",* Journal of the Optical Society of America Vol. 4, pp. 651 – 654

44) J. Durnin, J. J. Miceli, and J. H. Eberly, 1988, "*Comparison of Bessel and Gaussian beams.*", Optics Letters Vol. 13, pp. 79-80

45) J. P. Gordon, 1973, *"Radiation Forces and Momenta in Dielectric Media."*, Phys. Rev. A, Vol 8, pp.14

46) J. R. Moffitt, Y. R. Chemla, S. B. Smith, and C. Bustamante, 2008, "*Recent advances in optical tweezers*.", Annual Review of Biochemistry Vol. 77, pp. 205 – 228

47) Juozas Dudutis, Paulius GeČys, and Gediminas RaČiukaitis, 2016, *"Non-ideal axicon-generated Bessel beam application for intra-volume glass modification."*, Optics Express Vol. 24, pp. 28433-28443

48) C. Neuman and S. M. Block, 2004, "*Optical trapping.*", Rev. Sci. Instrum. vol. 75

49) K. Svoboda and S. M. Block, 1994, "*Biological applications of optical forces.*", Ann. Rev. Biophys. Biomol. Struct. Vol. 23, pp. 247 – 285

50) K. Visscher and G. J. Brakenhoff, 1992, "*Theoretical study of optically induced forces on spherical particles in a single beam trap I: Rayleigh scatterers*.", Optik Vol. 89, pp. 174 – 180

51) Karen Volke-Sepúlveda, Sabino Chávez-Cerda, Veneranda Garcés-Chávez, and Kishan Dholakia, 2004, "*Three-dimensional optical forces and transfer of orbital angular momentum from multiringed light beams to spherical microparticles.*", Journal of the Optical Society of America B Vol. 21, pp. 1749-1757

52)Giannelli, R. Betzholz, L. Kreiner, M. Bienert, G. Morigi, 2016, "*Laser and cavity cooling of a mechanical resonator with a Nitrogen-Vacancy center in diamond.",* arxiv.org: 1607.06656v2

53) Born and E. Wolf, 1975, "*Principles of Optics.",* Pergamon, London, pp. 437

54) M. de Angelis, A Bertoldi, L Cacciapuoti, A Giorgini, 2008, "*Precision gravimetry with atomic sensors.*", Meas. Sci. Technol. Vol. 20

55) M. J. Biercuk, H. Uys, J. W. Britton, A. P. VanDevender & J. J. Bollinger, 2010, "*Ultrasensitive detection of force and displacement using trapped ions."*, Nature Nanotechnology Vol. 5, pp. 646–650

56) M. J. Lang, C. L. Asbury, J. W. Shaevitz, and S. M. Block, 2002, "*An automated two-dimensional optical force clamp for single molecule studies.*", Biophys J. Vol. 83, pp. 491 – 501

57) M. K. Cheezum, W. F. Walker, and W. H. Guilford, 2001, "*Quantitative comparison of algorithms for tracking single fluorescent particles.*", Biophys J. Vol. 81, pp. 2378 – 2388

58) M. K. Zhou, Zhong-Kun Hu, Xiao-Chun Duan, Bu-Liang Sun, Le-Le Chen, Qiao-Zhen Zhang, and J. Luo, 2012, "*Performance of a cold-atom gravimeter with an active vibration isolator.",* Phys Rev A Vol. 86

59) M. Keller, J. Schilling, and E. Sackmann, 2001, "*Oscillatory magnetic bead rheometer for complex fluid microrheometry.*", Review of Scientific Instruments Vol. 72, pp. 3626

60) M. Kerker, 1969, "*The scattering of light and other electromagnetic radiation.",* Academic, New York, Chapter 3

61) M. L. Juan, C. Bradac, B. Besga, G. Brennen, G. Molina-Terriza, T. Volz, 2015, "*Observation of cooperatively enhanced atomic dipole forces from NV centers in optically trapped nanodiamonds.*", arxiv.org: 1511.04665

62) M. Lei and B. Yao, 2004, "*Characteristics of beam profile of Gaussian beam passing through an axicon.*", Opt. Commun. Vol. 239, pp. 367–372

63) M. Schmidt, 2011, "*A mobile high-precision gravimeter based on atom interferometry*.", Master's thesis, Humboldt University, Berlin

64) M. Schmidt, A. Senger, M. Hauth, C. Freier, V. Schkolnik, V. Schkolnik, 2011, "*A mobile high-precision absolute gravimeter based on atom interferometry.*", Gyroscopy Navig. Vol. 2, pp. 170

65) Marc Guillon, Olivier Moine, and Brian Stout, 2006, "*Longitudinal optical binding of high optical contrast microdroplets in air.*", phys. Rev. Lett. Vol 96

66) Maxwell J.C Treatise, 1873, "*Electricity and magnetism*.", Oxford, UK: Clarendon Press

67) McQueen, CA; Arlt, J; Dholakia, Kishan, 1999, "*An experiment to study a nondiffracting light beam.*", American Journal of Physics, Vol. 67, pp. 912-915

68) Romero-Isart, ML Juan, R. Quidant, and JI Cirac, 2010, "*Towards quantum superposition of living organisms.*", New J. Phys. Vol. 12

69) Oto Brzobohatý, Tomáš Čižmár, and Pavel Zemánek, 2008, "*High quality quasi-Bessel beam generated by round-tip axicon.", *Optics Express Vol. 16, pp. 12688-12700

70) Asenbaum, S. Kuhn, S. Nimmrichter, U. Sezer, M. Arndt., 2013, *"Cavity cooling of free silicon nanoparticles in high-vacuum.",* arXiv: 1306.4617

71) F. Barker and M. N. Shneider., 2010, *"Cavity cooling of an optically trapped nanoparticle.",* Phys. Rev. A, Vol. 81

72) P. F. Barker., 2010, *"Doppler Cooling a Microsphere.",* Phys. Rev. Lett. Vol. 105

73) P. M. Hansen, I. M. Toli-Nrrelykke, H. Flyvbjerg, and K. Berg-Srensen, 2006, "*tweezercalib 2.0: Faster version of MatLab package for precise calibration of optical tweezers.*", Computer Physics Communications Vol. 174

74) E. Thompson, D. R. Larson, and W. W. Webb, 2002, "*Precise nanometer localization analysis for individual fluorescent probes.*", Biophys. J., vol. 82

75) Grunwald, M. Bock, V. Kebbel, S. Huferath, U. Neumann, G. Steinmeyer, G. Stibenz, J.-L. Néron, and M. Piché, 2008, "*Ultrashort-pulsed truncated polychromatic Bessel-Gauss beams.*", Opt. Express Vol. 16, pp. 1077–1089

76) R. M. Herman and T. A. Wiggins, 1991, *"Production and uses of diffractionless beams.",* Journal of the Optical Society of America A, Vol. 8, pp. 932-942

77) R. Omori, T. Kobayashi, and A. Suzuki, 1997, *"Observation of a single-beam gradient-force optical trap for dielectric particles in air."*, Optics Letters Vol. 22, pp. 816-818

78) R. P. MacDonald, S. A. Boothroyd, T. Okamoto, J. Chrostowski, B. A. Syrett, 1996, *"Interboard optical data distribution by Bessel beam shadowing, Optics Communications.",* Vol. 122, pp. 169-177

79) Akturk, 2012, *"Tailored-beam ultra-short laser pulses.",* Quantum Phys. Lett. Vol. 112, pp. 97–112

80) S. Chu, J. E. Bjorkholm, A. Ashkin, and A. Cable, 1986, *"Experimental Observation of Optically Trapped Atoms."*, Phys. Rev. Lett. Vol. 57, pp. 314

81) S. Chu, L. Hollberg, J. E. Bjorkholm, A. Cable, A. Ashkin, 1985, *"Three-dimensional viscous confinement and cooling of atoms by resonance radiation pressure.",* Phys. Rev. Lett. Vol. 55, pp. 48–51

82) S. Monk, J. Arlt, D.A Robertson, J Courtial, M.J Padgett, 1999, "*The generation of Bessel beams at millimeter-wave frequencies by use of an axicon.*", Volume 170, 1, pp. 213–215

83) Li, 2013, "*Fundamental Tests of Physics with Optically Trapped Microspheres.*", Springer

84) T. Li, S. Kheifets, and M. G. Raizen., 2011, *"Millikelvin cooling of an optically trapped microsphere in vacuum.",* Nature Physics Vol. 7, pp. 527–530

85) Tongcang Li, Simon Kheifets, David Medellin, and Mark G. Raizen. 2010*, "Measurement of the Instantaneous Velocity of a Brownian Particle*.", Science Vol. 328, pp. 1673

86) Daria, J. Glückstad, 2005, *"Four-dimensional optical manipulation of colloidal particles."*, Rodrigo, Appl. Phys. Lett. Vol. 86

87) Jarutis, R. Paškauskas, and A. Stabinis, 2000, "*Focusing of Laguerre-Gaussian beams by axicon.*", Opt. Commun. Vol. 184, pp. 105–112

88) R. Bowman, N. Muller, X. Zambrana-Puyalto, O. Jedrkiewicz, P. Di Trapani, M. J. Padgett, 2011, "*Efficient generation of Bessel beam arrays by means of an SLM.",* The European Physical Journal Special Topics Vol. 199, pp. 159-166

89) Harada, T. Asakura, 1996, *"Radiation forces on a dielectric sphere in the Rayleigh scattering regime."*, Optics Communications Vol. 124, pp. 529-541

90) Lin, W. Seka, J. H. Eberly, H. Huang, and D. L. Brown, 1992, *"Experimental investigation of Bessel beam characteristics.",* Applied Optics Vol. 31. Pp. 2708-2713

91) Zhang-qi Yin, 2009, *"Phase noise and laser-cooling limits of optomechanical oscillators.",* Phys. Rev. A, Vol. 80

92) Zhang-qi Yin, Tongcang Li, and M. Feng, 2011, *"Three-dimensional cooling and detection of a nanosphere with a single cavity."*, Phys. Rev. A Vol. 83

Appendix

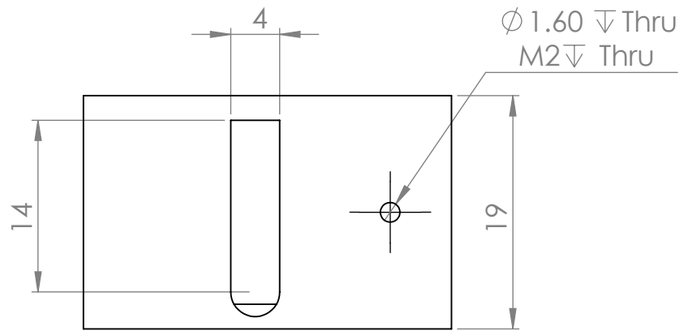

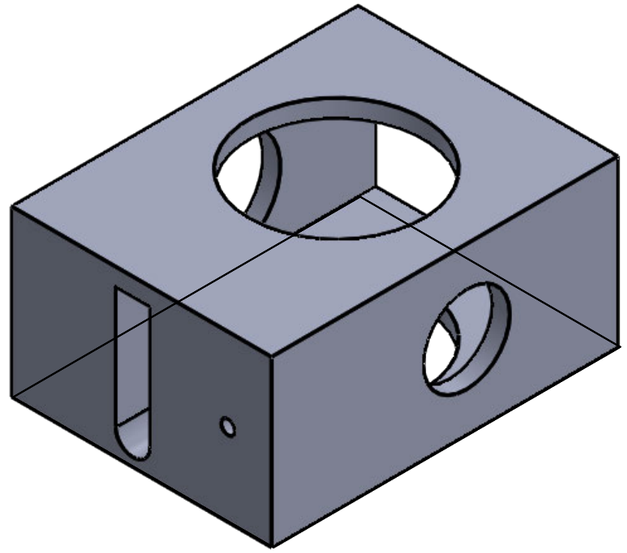

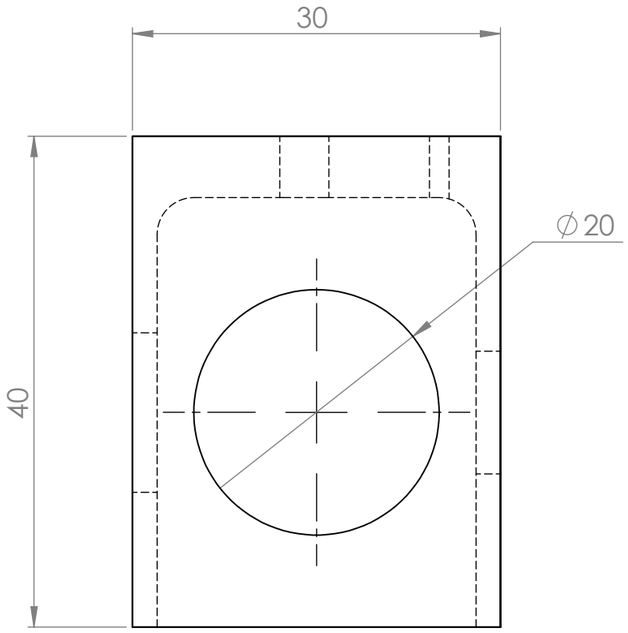

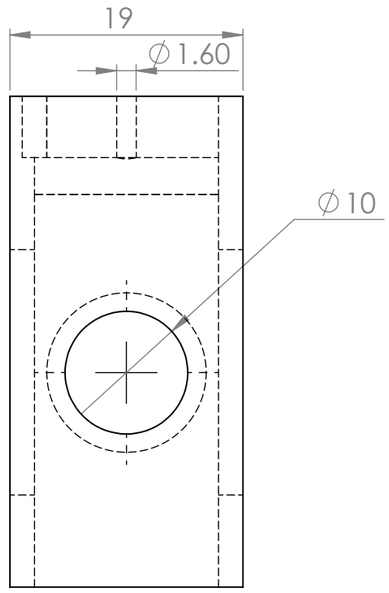

SOLIDWORKS Educational Product. For Instructional Use Only.

UNLESS OTHERWISE SPECIFIED: DIMENSIONS ARE IN MILLIMETERS SURFACE FINISH: TOLERANCES: LINEAR: ANGULAR:		FINISH:		DEBURR AND BREAK SHARP EDGES		DO NOT SCALE DRAWING	REVISION
	NAME	SIGNATURE	DATE			TITLE:	
DRAWN	Md Iftekher Selim Chowdhury						
CHK'D							
APPV'D							
MFG							
Q.A				MATERIAL:		DWG NO.	A3
						Trapping Chamber	
				WEIGHT:		SCALE:2:1	SHEET 1 OF 1